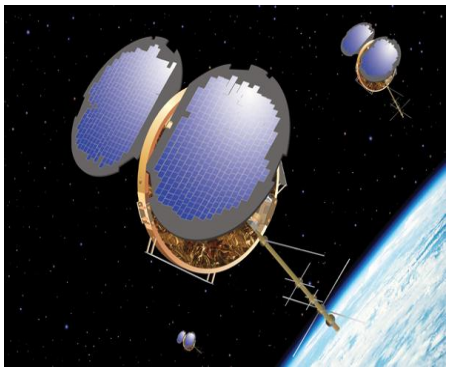

COSMIC

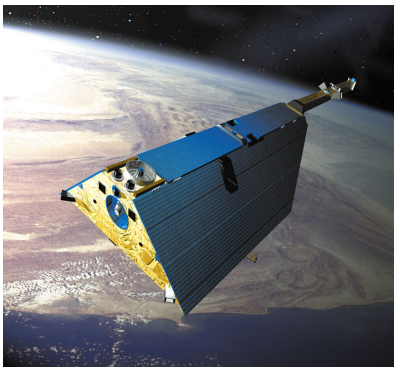

CHAMP

YEAR 2 BI-ANNUAL PROJECT REPORT (from 06/01/2011 to 12/31/2011)
NOAA Award number: NA10NES4400002

Construction of Consistent Microwave Sensor Temperature Records and Tropopause Height Climatology using MSU/AMSU Measurements, GPS RO Data, and Radiosonde Observations

Principal Investigator:
Shu-Peng (Ben) Ho (303-497-2922, spho@ucar.edu)

Co-Investigators:
Cheng-Zhi Zou ((301) 763-8042 x156, cheng-zhi.zou@noaa.gov)
Ying-Hwa Kuo ((303) 497-8910, kuo@ucar.edu)

National Center for Atmospheric Research
P.O. Box 3000, Boulder, CO 80307 USA

1. Introduction

In previous reports, we have summarized research results for

> i) using GPS RO soundings collected from multi-RO missions but processed using a consistent processing package to construct tropopause height climatology from 2001 to 2012 that is consistent with changes in temperature and tropopause structure estimated by radiosondes, and
>
> ii) using GPS RO data from 2001 to 2012 as climate benchmark datasets to quantify the Microwave Sounding Unit (MSU)/Advanced Microwave Sounding Unit (AMSU) temporal and spatial temperature anomalies. Doing so would help define a better approach for constructing MSU/AMSU temperature records from 1979 to 2012.

During this performance period (form June to December 2011), we have focused on using CHAMP RO data processed by six RO operational centers to quantify structural uncertainty of RO derived atmospheric variables and examine their suitability for climate monitoring. While the fundamental phase delay observed from the GPS RO technique is synchronized to the ultra-stable atomic clocks on the ground, the derived RO variables (e.g., bending angle, refractivity, temperature, geo-potential height, and temperature profiles) are not. The retrieved results may vary when different processing algorithms and implementations are used. To use RO derived temperature profiles to calibrate AMSU/MSU data, we will need to quantify the structural uncertainty of RO data.

In this study, profile-to-profile CHAMP variables from January 2002 to September 2008 retrieved from common approaches but different implementations among centers are compared. Profile-to-profile CHAMP variables from January 2002 to September 2008 retrieved by the six centers are compared. The work undertaken to date on these project goals is detailed in section 2, and related presentations and publications from January 2011 to December 2011 are listed in section 3.

2. Progress on Proposed Studies

2.1 Preparation of GPS RO for Geo-location Comparisons

a. Data collection

Currently, multi-year GPS RO data can be obtained from :

- The GeoForschungsZentrum Potsdam (GFZ), Germany,
- the Jet Propulsion Laboratory (JPL), Pasadena, CA, USA,
- University Corporation for Atmospheric Research (UCAR), Boulder, CO, USA, and

- the Wegener Center of the University of Graz (WEGC), Graz, Austria,
- European Organisation for the Exploitation of Meteorological Satellites (EUM),
- Darmstadt, Germany, and Danish Meteorological Institute (DMI), Copenhagen, Denmark.

These centers used different assumptions, initializations, and implementations in the excess phase processing and inversion procedures. Recently, Ho et al., (2009, hereafter Ho2009) used five years (2002–2006) of refractivity monthly mean climatology (MMC) from CHAMP generated by the above GFZ, JPL, UCAR, and WEGC to find out to what extent retrieval error is systematic in time and can be expected to cancel in trend estimation. Each center used the profiles passing their own quality control criteria to generate their own MMCs. Results showed that the uncertainty of the trend for fractional refractivity anomalies among centers is between -0.03 to 0.01%/5 years. Thus 0.03%/5 years can be considered an upper bound in the processing scheme-induced uncertainty for global refractivity trend monitoring.

In that study, because different implementations of quality control have the effect of eliminating different subsets of the entire data set, the sampling errors are still the dominant error source. Although re-analysis data were used to determinate sampling errors among centers, we still cannot distinguish if the remaining differences among centers are due to residual sampling errors or inversion related structural uncertainty. The structural uncertainties among centers are still not understood. Here we conduct profile-to-profile (i.e., no sampling differences) RO sounding (bending angle, refractivity, and temperature) comparisons among all six centers. This should help to identify the causes of process-dependent errors from each center.

CHAMP RO data used in this study are collected from the following sources:

- CHAMP profiles from GFZ used in this study have been reprocessed with the latest version (006) of GFZ's operational occultation analysis system. It is planned to provide these data via the Information System and Data Center (ISDC, http://isdc.gfz-potsdam.de). Details and related references on the operational standard near-real time orbit and occultation processing can be found in König et al. (2006) and Wickert et al. (2009).

- CHAMP profiles from JPL were downloaded from the JPL Genesis website, http://genesis.jpl.nasa.gov. The inversion procedures used to process CHAMP data for this study are the same as those used in Ho2009.

- UCAR operational CHAMP profiles (version 2009.3140) were downloaded from the UCAR COSMIC Data Analysis and Archive Center (CDAAC) http://cosmic-io.cosmic.ucar.edu/cdaac/index.html. An updated POD code is developed and implemented in this version (Schreiner et al., 2009, also see section 2.2). A general description of UCAR inversion procedures can be found in Kuo et al., (2004), Ho2009, and Schreiner et al., (2011).

- RO atmospheric profiles provided by the Wegener Center were retrieved with the WEGC Occultation Processing System (OPS) retrieval software (*Borsche et al*., 2006; *Kirchengast et al.*, 2007; *Borsche*, 2008; *Foelsche et al*., 2008; 2009; *Ho*2009). A short overview on the current retrieval version OPSv5.4 is given by *Steiner et al.* (2009), a detailed description can be found in *Pirscher* (2010). The WEGC OPSv5.4 retrieval is a dry air geometric optics retrieval based on input data of RO phase and orbit information provided by the UCAR CDAAC. WEGC profile data and climatology data are available from its global climate monitoring website, http://www.wegcenter.at/globclim. Information on error characteristics is given by *Scherllin-Pirscher et al*. (2011a; 2011b).

- EUM and DMI constructed the CHAMP retrievals specifically for this study. Like WEGC, both EUM and DMI started with excess-phase and amplitude data, and CHAMP orbital data, from the UCAR CDAAC. These data are processed with the UCAR procedure described in Section 2.2.d. EUM only provided bending angle profiles for this study.

b. Inversion Procedures applied for CHAMP RO Data at GFZ, DMI, EUM, JPL, UCAR, and WEGC

Accurate RO retrievals of atmospheric variable profiles depend on the adequate calculation of the GPS excess atmospheric phase data of two L band frequencies (1575.42 MHz (L1) and 1227.6 MHz (L2)) due to signal delay and bending in the Earth's atmosphere and ionosphere (Kursinski et al., 1997; Ho et al., 2009a). Possible error sources of RO derived products include i) observation errors and ii) inversion errors. Observation errors are errors in RO phase measurements, which is related to GPS RO signal strength combined with receiver noise for a particular RO mission, local multipath effect, and so on.

Though implementation of these procedures by different processing centers is different, the main processing steps are, to a large extent, common. These steps include:

i) RO atmospheric excess phase processing,
ii) POD and clock synchronization,

iii) The procedure to retrieve bending angle from the Doppler measurement,
iv) The extrapolation of the ionospheric correction into the lower troposphere, necessary because of the influence of the ionosphere on measured phase delay of GPS signals,
v) The initialization of the Abelian integral transform to convert atmospheric bending angles to profiles of refractivity,
vi) The procedure to derive dry temperature and dry pressure, which are obtained in the upper troposphere by assuming a completely dry atmosphere,
vii) The procedure to derive geo-potential height, and
viii) Quality control procedures for above steps.

c. Matching of CHAMP Profiles from Each Individual Centers and Preparation of CHAMP Monthly Mean Climatologies

The inter-center comparisons are based on statistical differences of profile-to-profile pairs of bending angle, refractivity, temperature, dry pressure, and geo-potential height profiles. The following procedures are used to matching CHAMP profiles from each individual centers:

i) The profile-to-profile comparisons (PPCs) were first obtained by matching the profiles produced by all 6 centers;
ii) Each center supplied CHAMP processed profiles from January 2002 to August 2008 in a common netCDF file format;
iii) The occultation time and occulting GPS satellite identifiers from each profile were then compared with a database of all geometrically possible occultations to obtain standard occultation times;
iv) The provided profile files from each center were then given canonical names using the standard occultation times. Only profiles from individual centers that passed their QCs for all retrieved variables are included in the common ppc files.

This matching was done within a 5-minute time window for occultations using the same GPS satellite. In this way the profile files from all centers were matched up and assigned common occultation identifiers. The vertical resolution of RO data is from ~300 m near the surface to ~1.5 km at 40 km. All the centers provided their RO data products on a fixed vertical grid of 200 meter from 8 km to 30 km.

2.2 Quantification of the Reproducibility of RO Data for Climate Monitoring

To quantify the latitudinal and temporal comparisons of inter-center differences, we further compare the monthly mean climatologies (MMC) of the common set of CHAMP profiles. In the common set of CHAMP profiles, the sampling errors due to temporal and spatial mismatches among individual centers are eliminated. We group the matched profiles from all six centers in zonal bins of 5° latitudinal width

(i.e., 36 bins). An evenly spaced 200 m vertical Mean Sea Level (MSL) grid is used. CHAMP data processed independently by the six centers in the period from Jan 2002 to August 2008 are used to generate the MMCs.

a. Global Anomaly Comparison Among Centers

- Method: The RO anomalies of RO derived variables are computed using the following equation:

$$\Delta X^{PPC}(j) = 100\% \times (1/n) \times \sum_{l=1}^{l=n} \{X^{PPC}(l,j) - Mean_X^{PPC}(l,j)\} / Mean_X^{PPC}(l,j), \qquad (1)$$

- Here *j* is index of vertical grid from 8 km to 30 km at a 200-meter vertical grid from January 2002 to August 2008, and *l* is index for all the matched pairs at vertical grid *j*. $X^{PPC}(l,j)$ and $Mean_X^{PPC}(l,j)$ are RO-derived variable profile and the mean variable of all six centers for matched pair *l* at vertical grid *j*.

- Figure 1 depicts the global bending angle anomalies for DMI, EUM, GFZ, JPL, UCAR, and WEGC (i.e., ΔB_{DMI}^{PPC}, ΔB_{EUM}^{PPC}, ΔB_{GFZ}^{PPC}, ΔB_{JPL}^{PPC}, ΔB_{UCAR}^{PPC}, ΔB_{WEGC}^{PPC}, respectively). The mean differences from the 8 km to 30 km layer and the median absolute deviation (MAD) in the same height range are shown in Figure 1.

- Results shown here demonstrated that the mean ΔB for all matched pairs among centers agree to within ±0.04% (where the mean ΔB_{JPL}^{PPC} from 2002 to 2008 are equal to 0.04 % and that for WEGC is equal to -0.03%).

- The MAD for DMI, EUM, GFZ, JPL, UCAR, and WEGC anomalies from the inter-center mean for the 8-30 km layer are 0.47%, 0.63%, 0.51%, 0.74%, 0.34%, and 0.32%, respectively.

- The bias below 13 km is probably due differences in the approach for downward extrapolation of L1-L2 for ionospheric correction. Especially the choice of the data interval used for extrapolation is different between the centers and may introduce differences in the observed magnitude.

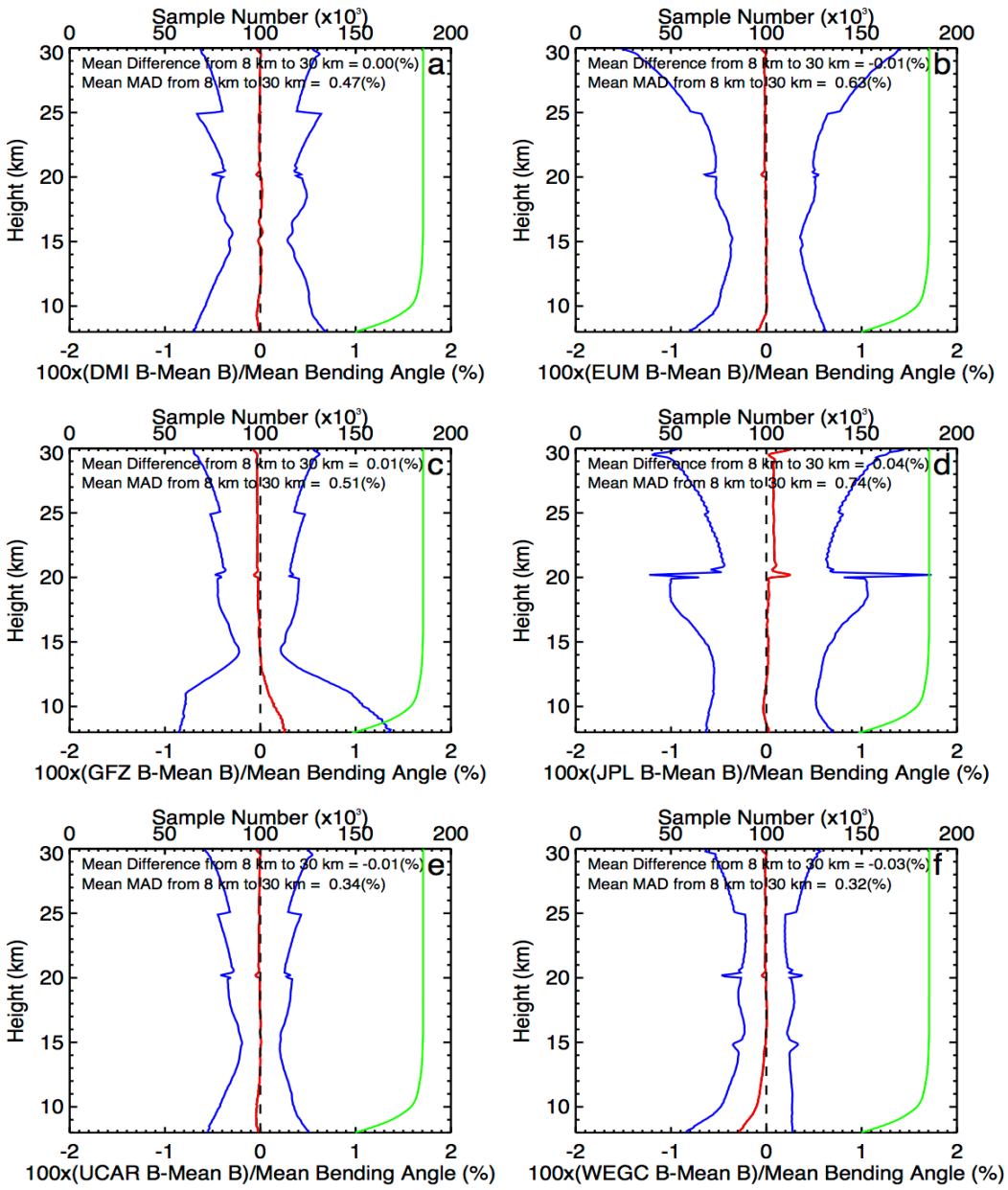

Fig. 1. The mean and standard deviation of global bending angle anomalies for (a) DMI, (b) EUM, (c) GFZ, (d)JPL, (e) UCAR, and (f) WEGC from the January 2002 to August 2008. The red solid line is the mean anomalies, the blue line is the standard deviation to the mean anomalies, and the green line is the number of the matched pairs.

b. Comparison of Zonal Average Anomalies Among Centers

- Method: here we use the following equation to generate zonal average anomalies for RO derived variables for individual centers:

$$\Delta X(i,j) = (1/80) \times \sum_{k=1}^{k=80} \{MMC_X(i,j,k) - \overline{MMC_X}(i,j,k)\} \ , \qquad (2)$$

  where *i* is the index of latitude bins (5-degree), *j* is the index for the altitude bins (200-meter form 8 km to 30 km), and *k* is the month index (from January 2002 to August 2008). $\overline{MMC_X}(i,j,k)$ is the mean of MMC of the compared variable for all centers (inter-center mean) in each latitude, height, and month bin.

- Figure 2 depicts the mean fractional refractivity anomalies for 2007 for each of the five centers (i.e., ΔN_{DMI}, ΔN_{GFZ}, ΔN_{JPL}, ΔN_{UCAR}, and ΔN_{WEGC} where EUM has no refractivity products) with the inter-center mean removed. The patterns of the mean fractional refractivity anomalies for other years are similar to this year and are not shown.

- In general, the fractional refractivity anomalies for all centers are within ±0.2% except for GFZ near the equator below 10 km.

- The slightly positive ΔN_{JPL} above 10 km along all latitudes may be the result of the global positive bending angle anomalies (~0.04%), shown in Figure 2d.

- The slightly positive ΔN_{UCAR}, ΔN_{DMI}, and ΔN_{WEGC} above 15 km south of 50° S are compensating the negative ΔN_{GFZ} in the same region. ΔN_{GFZ} has an obvious latitudinal bias relative to the inter-center mean (Figure 4b). ΔN_{GFZ} has an about -0.2% bias above 20 km altitude in the southern mid-latitude and polar region while it has a 0.2% bias in the northern polar region above the same altitude.

- These biases (not observed in the raw bending angels) are related to GFZ's approach of bending angle initialization, especially the stronger weighting of RO measurements with respect to background information. The biases are obviously connected with a different trend behavior of GFZ's refractivity data in these regions.

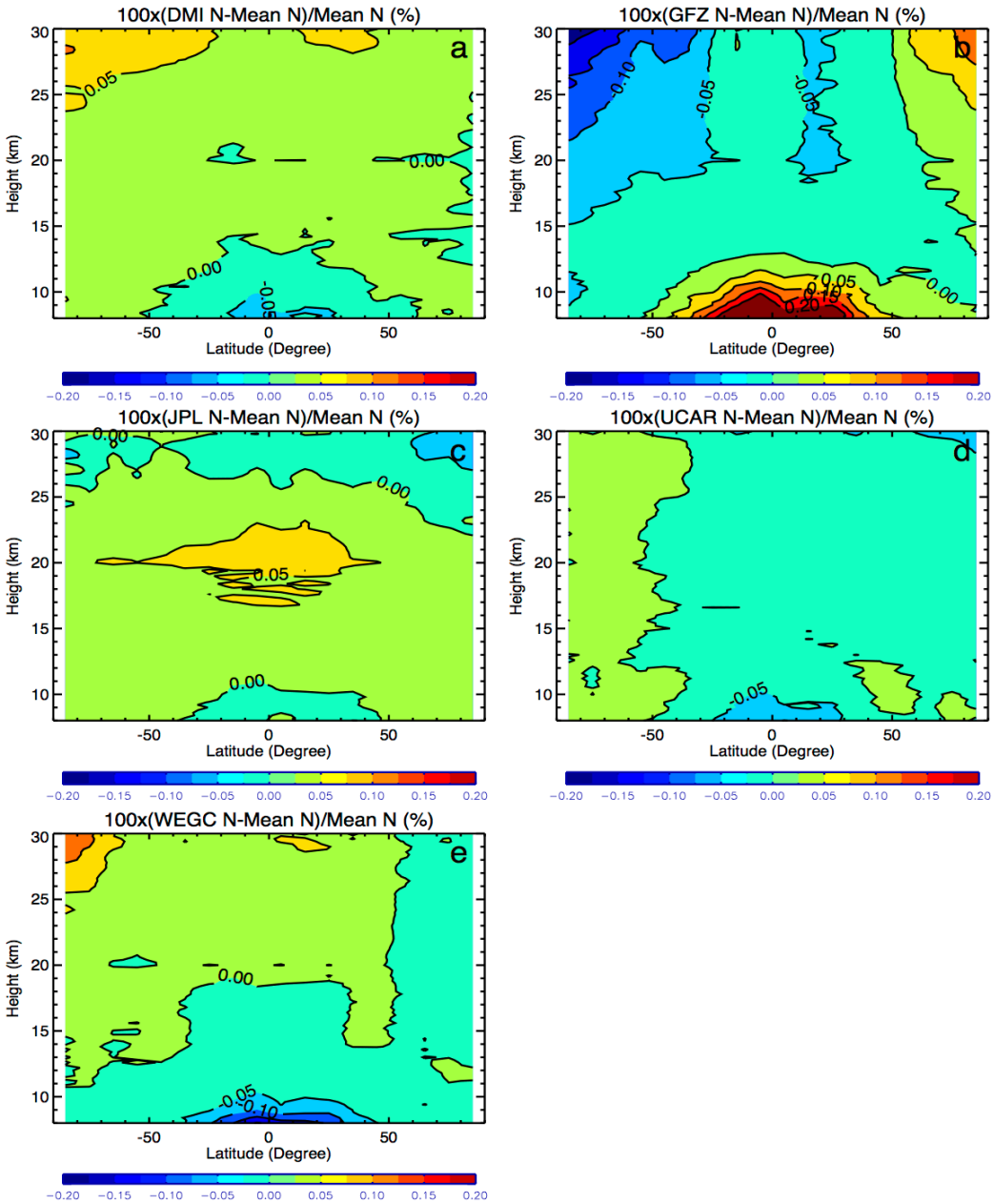

Fig. 2 The difference in the mean zonal-average fractional refractivity from the inter-model mean over the period from January 2002 to August 2008, for each of the five contributing processing centers: (a) DMI, (b) GFZ, (c) JPL, (d) UCAR, and (e) WEGC.

- The corresponding two-dimensional distribution of the MAD of the fractional refractivity anomalies (e.g., ΔN_{DMI}^{MAD}, ΔN_{GFZ}^{MAD}, ΔN_{JPL}^{MAD}, ΔN_{UCAR}^{MAD}, and ΔN_{WEGC}^{MAD}) is shown in Figure 3.

- It illustrates that even with different inversion procedures to convert raw phase data to bending angles and refractivity, the MAD of the fractional refractivity anomalies among centers are in general smaller than 0.25 % below 25 km at all latitudes. This is also partially reflecting the high precision of RO data (~0.1 K in temperature and ~0.05% in fractional refractivity, e.g., Ho2009).

- The ΔN_{DMI}^{MAD}, ΔN_{UCAR}^{MAD}, and ΔN_{WEGC}^{MAD} are all as small as 0.2% from 8 km to 30 km at all latitudes, which again may result in the fact that all these three centers were using the same phase and orbit data from UCAR.

- The differences among ΔN_{GFZ}^{MAD}, ΔN_{JPL}^{MAD}, and ΔN_{UCAR}^{MAD} may reflect the upper bound uncertainty by using different orbit data and inversion procedures.

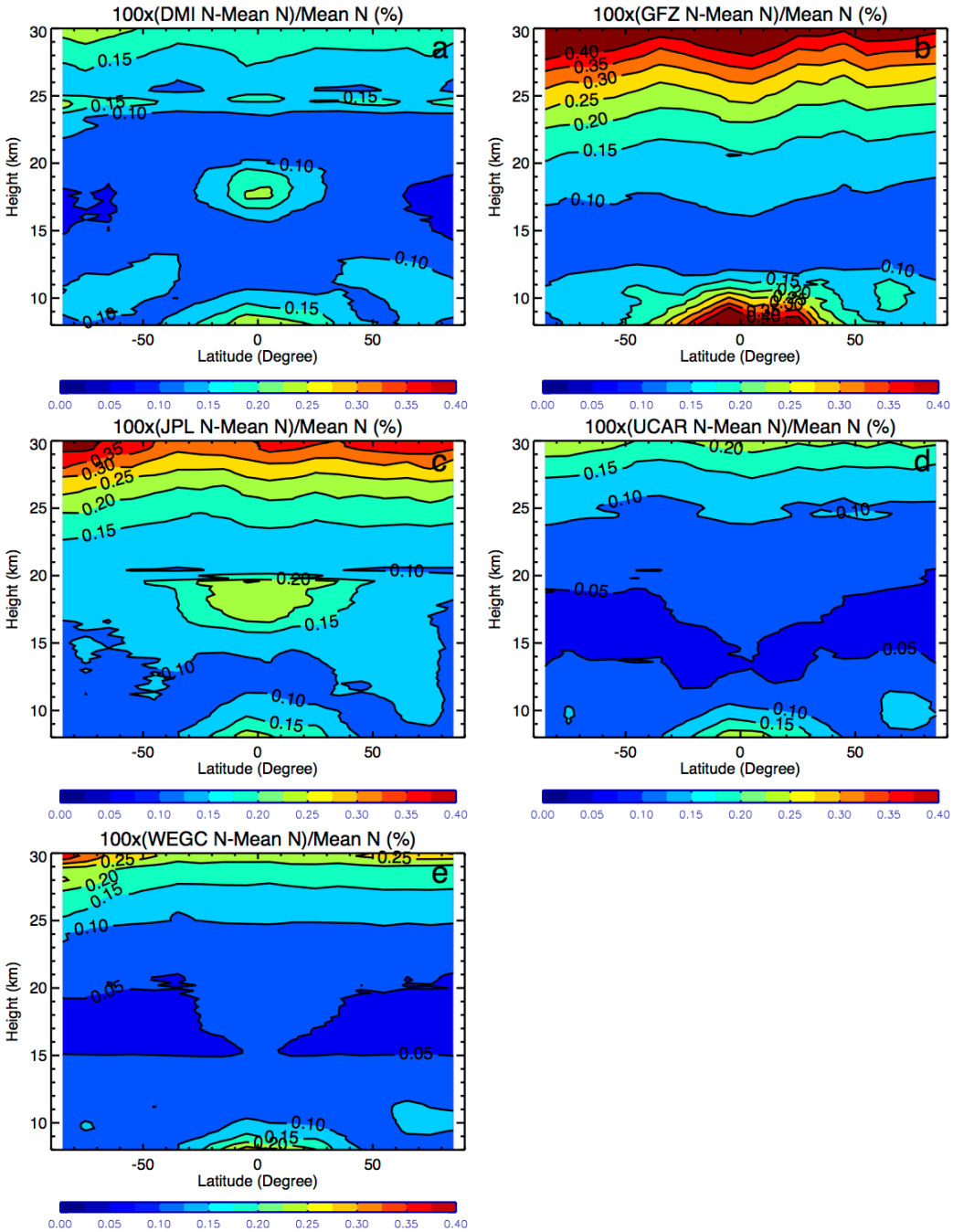

Fig. 3 The Median Absolute Deviation (MAD) of the fractional refractivity anomalies in the period January 2002 to August 2008 to their mean from all five centers in the same period for (a) DMI, (b) GFZ, (c) JPL, (d) UCAR, and (e) WEGC.

c. Time Series Comparison of Retrieval Anomalies

- To further quantify the reproducibility/consistency of the CHAMP data processed from different centers we compare the time dependent anomalies among centers. The following equation is used to calculate the time series anomalies for RO variables:

$$\Delta X^{Time}(l,m,k) = MMC_X(l,m,k) - \overline{MMC_X^{Time}}(l,m,k), \qquad (3)$$

  where *l* is the index for different vertical layers including the 8-30 km layer, the upper troposphere (UT, the 8-12 km layer), the lower stratosphere layer (LS, the 12-20 km layer), and the mid-stratosphere (MS, the 20-30 km layer). We construct the time series comparisons in six latitudinal zones (*m*) including global, (from 87.5º N to 87.5º S), northern high-latitudes (from 87.5º N to 60º N), sub-tropical and northern mid-latitudes (from 60º N to 20º N), Tropics (20º N to 20º S), sub-tropical and southern mid-latitudes (from 20º S to 60º S), and southern high-latitudes (from 60º S to 87.5º S). *k* is index of monthly bin (k =1, 80) and $\overline{MMC_X^{Time}}(l,m,k)$ is the inter-center mean MMC for each layer-, zone-, and month-bin. The MMC fractional anomaly time series for bending angle (%), refractivity (%), and dry pressure (%) are computed.

- Figure 4 depicts the MMC fractional bending angle anomaly time series for DMI, EUM, GFZ, JPL, UCAR, and WEGC for the 8-30 km layer (i.e., ΔB_{DMI}^{Time}, ΔB_{EUM}^{Time}, ΔB_{GFZ}^{Time}, ΔB_{JPL}^{Time}, ΔB_{UCAR}^{Time}, ΔB_{WEGC}^{Time}) with inter-center mean removed at all six latitudinal zones, Figure a for the global, and Figures b-f for the northern high-latitudes, sub-tropical and northern mid-latitudes, Tropics, sub-tropical and southern mid-latitudes, and southern high-latitudes, respectively.

- All these Figures present similar qualitative features:
  (1) the anomalies from individual center are persistent in time and there is no obvious latitudinal dependent biases except for ΔB_{GFZ}^{Time} in the tropical region (~0.29%, Fig. 4d) and small ΔB_{JPL}^{Time} in the northern high-latitudes (~0.14%) and in the southern high-latitudes (~ -0.17%), and

  (2) individual center's anomalies are of no obvious inter-monthly and inter-seasonally variance except for small ΔB_{GFZ}^{Time} in the Tropics (the standard deviation is ~0.06%), southern and northern mid-latitudes (the standard deviation is ~0.07%).

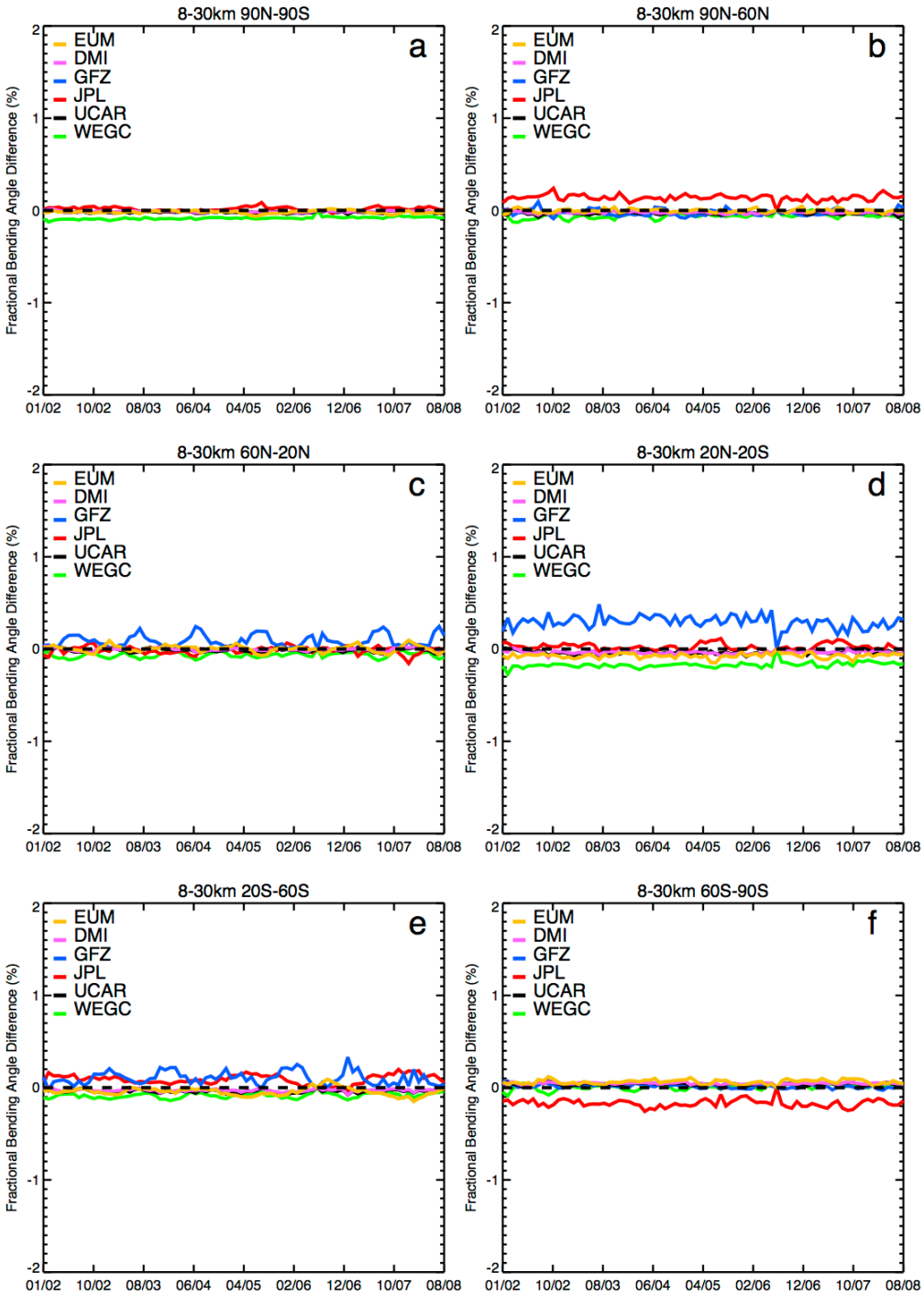

Fig. 4. The time series of fractional bending angle anomalies among five centers for the 8-30 km layer for (a) the entire globe (90ºN-90ºS), (b) the 90ºN-60ºN zone, (c) the 60ºN-20ºN zone, (d) the 20ºN-20ºS zone, (e) the 20ºS-60ºS zone, and (f) the 60ºS-90ºS zone. The inter-model mean was subtracted on a monthly basis.

- The time series of fractional refractivity anomalies (ΔN^{Time}) also show similar qualitative features to that of ΔB^{Time} except with a different magnitude. The mean global biases among centers in the 8-30 km layer are within ±0.03% with a close to 0.01% standard deviation.

- Figure 5 depicts ΔN^{Time} for five individual centers (no EUM) in the mid-latitudes, the Tropics, and the southern high-latitudes, Figures 5 a, c, and e for the 8-12 km layer, and Figures 5 b, d, and f for the 20-30 km layer.

- The anomalies from individual centers are in general persistent in time except for the northern mid-latitudes in the 8-12 km layer (Fig. 5a). A 0.65% of fractional bending angle bias (e.g., ΔB_{GFZ}^{Time} in the Tropics for the 8-12 km layer) is likely leading to a ~0.1% of fractional refractivity bias (e.g., ΔN_{GFZ}^{Time}).

- Note that, as mentioned in Ho2009, because the inter-center mean is subtracted, results from each center need to offset the persistent or varying anomalies from an individual center with compensating behavior. The magnitude of the mean anomalies is merely used to indicate the deviation of individual center to the inter-center mean but the accuracy of the time series.

- Here we focus on quantifying the systematic inter-center difference and inter-monthly variance among centers. The obvious inter-seasonal bias for ΔN_{GFZ}^{Time} in the sub-tropical and mid latitudes in the 8-12 km layer reflects the behavior of bending angle bias in these regions.

- The increasing negative fractional refractivity for GFZ over southern high-latitudes in the MS region after the end of 2004 is related to GFZ's approach of bending angle initialization, especially the stronger weighting of RO measurements with respect to background information. In fact this negative trend disappears if the original observation error variance is used.

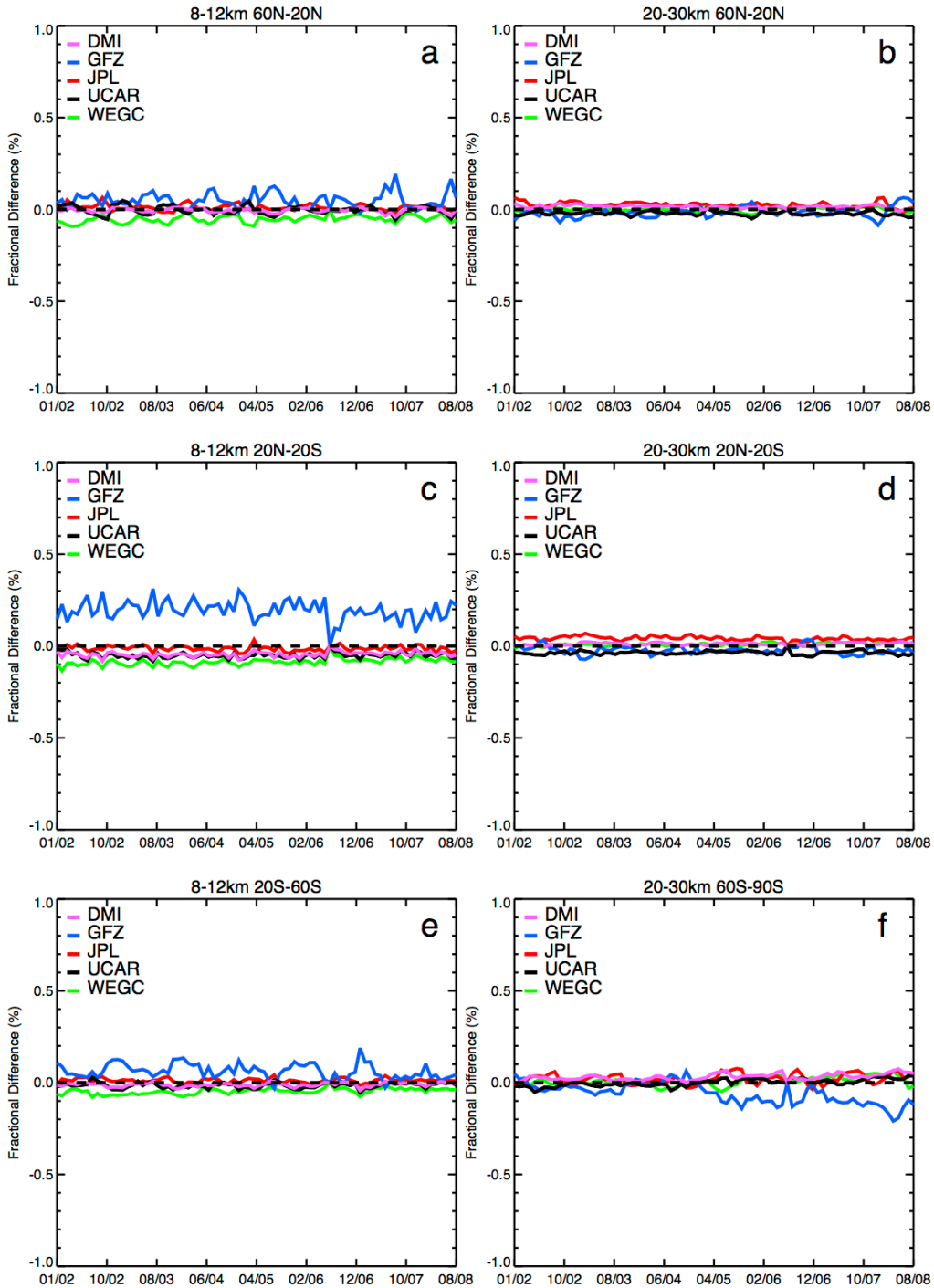

Fig. 5. The time series of fractional refractivity anomalies among five centers for the 8-12 km layer for (a) the 20ºN to 60ºN zone, (c) the 20ºN to 20ºS zone, and (e) the 60ºS to 90ºS zone, and in the 20-30 km layer for (b) the 20ºN to 60ºN zone, (d) the 20ºN to 20ºS zone, and (f) the 60ºS to 90ºS zone.

d. Trends and Variability in Anomalies

- Here we aim to quantify trends and anomalies of the de-seasonalized GPS RO derived variables from six centers. While Ho2009 used 5 years of RO data, here we use nearly 7 years (80 months in total) of RO matched pairs. The following equation is used to derive the de-seasonalized MMC anomaly:

$$\Delta X^{Deseason}(k,m,l) = MMC_X(k,m,l) - \overline{\overline{MMC_X}}(k,m,l'), \qquad (4)$$

  where *k*, *m* , and *l* are the indices of the month bin for each layer (*k*), zone (*m*) and month for the whole time series (*l* = 1 to 80), respectively, and l' is the index of the month bin of the year (l' =1 to 12). $\overline{\overline{MMC_X}}(k,m,l')$ is the mean MMC for each layer (*k*), zone (*m*), and averaged over all years for a particular month (l'). Here the $\overline{\overline{MMC_X}}(k,m,l')$ is computed for the period from January 2002 to December 2005 since the MMC for July 2006 is not available. The mean trends of all centers and the trend difference to the mean trend for each individual center are summarized in Tables 3-7 for fractional bending angle, fractional refractivity, dry pressure, temperature, and geo-potential height in each latitudinal zone and vertical layer.

- Fig. 6 depicts the de-seasonalized fractional refractivity anomalies for each center in southern high-latitude, Tropics, and northern mid-latitude zones, left panels are for the 12-20 km layer and the right panels are for the 20-30 km layer.

- In general, the trend differences in the 12-20 km layer in all latitudinal zones are very close to zero, except for in the southern mid-latitudes (Table 4). In this region, the trend difference to the mean trend for GFZ is equal to -0.02%/5 yrs where those for all other centers are equal to 0.01%/ 5yrs. Over Tropics in the MS region, the trend differences among centers are within ± 0.01%/5 yrs.

- This relatively large trend difference for GFZ in this region is mainly due to the large negative fractional refractivity anomalies (ΔN_{GFZ}^{Time}) after 2004 (Fig. 6f). This is more pronounced in the temperature trend differences (see below).

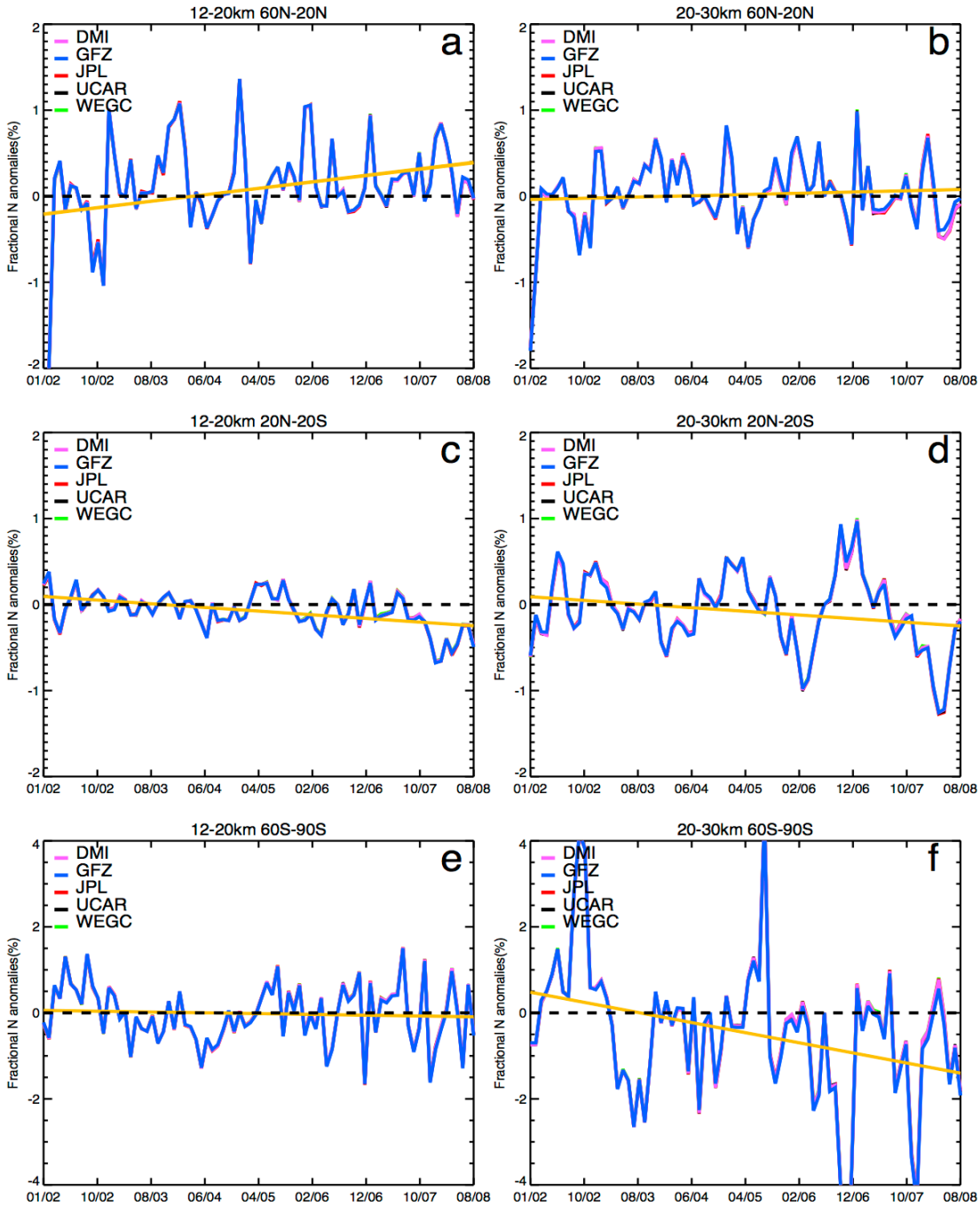

Fig. 6 The de-seasonalized fractional refractivity anomalies for each center in the 12-20 km layer for (a) the 20ºN to 60ºN zone, (c) the 20ºN to 20ºS zone, and (e) the 60ºS to 90ºS zone, and in the 20-30 km layer for (b) the 20ºN to 60ºN zone, (d) the 20ºN to 20ºS zone, and (f) the 60ºS to 90ºS zone. The 5-yr trend for UCAR is shown as well. Note that panels e and f have its ordinate range enlarged to +/-4% (relative to +/-2% of panels a-d).

e. Conclusions

This study has utilized CHAMP RO data processed by six RO operational centers to quantify structural uncertainty RO derived atmospheric variables and examine their suitability for climate monitoring. Our analyses reach the following conclusions:

- Although the PPC results cannot be used to indicate the accuracy of retrieved variables derived by individual centers, the mean differences and the standard deviations relative to the inter-center mean give us the structural uncertainty among centers due to different implementations and processing assumptions used in the RO inversion procedures along the processing chain.

- Results show that despite different implementations in the inversion procedures among centers, the global mean bending angle differences from the 8-30 km layer from 2002 to 2008 are within ±0.04%, where JPL (e.g., ΔB_{JPL}^{PPC}) gives an upper bound for 0.04% and that for WEGC is equal to -0.03%.

- The large deviation of ΔB_{JPL}^{PPC} mainly above 20 km of altitude may be related to the fact that all centers incorporate MSIS climatology in some form for the initialization, except for JPL. The 0.04% of ΔB_{JPL}^{PPC} leads to mean JPL anomalies equaling to 0.02%, -0.27K, -0.11%, and -0.01 km for fractional refractivity, temperature, dry pressure, and geo-potential height in the same layer, respectively.

- The mean bending angle MADs for EUM, DMI, GFZ, JPL, UCAR, and WEGC for the same time period for the 8 to 30 km layer are as small as 0.63%, 0.47%, 0.51%, 0.74%, 0.34%, and 0.32%, respectively.

- RO retrieval errors are mainly form the combined contribution of the observational errors (including thermal error due to signals to noise ratio, local multipath), calibration errors (ionopheric correction for solar maximum), and inversion errors (Abel boundary effect, etc). In this study, the observational errors are common errors among centers, and the structural uncertainties among centers are mainly from both calibration errors and inversion errors. Although cannot distinguish the detail error budgets caused in each processing step, the PPC results show that the variation of standard deviation with height for all the derived variables and the propagation of the errors in the processing chain are very consistent with (and sometimes smaller than) those from theoretical analysis estimated by Kursinski1997.

- The standard deviation of all the variables is smallest near the 15 km and grows exponentially near 30 km. The estimated standard

deviations near the 15 km vary slightly among centers and the mean standard deviation from all centers near 15 km for fractional bending angle, fractional refractivity, temperature, fractional pressure, and geo-potential height are within 0.5%, 0.1%, 0.3K, 0.02%, and 10 m, respectively. The gives us confidences to use RO for climate monitoring as claimed by Kursinski1997.

- Although there are small mean anomalies among centers, those anomalies are more or less systematic in the time series comparisons. The mean bias for ΔB_{DMI}^{Time}, ΔB_{EUM}^{Time}, ΔB_{GFZ}^{Time}, ΔB_{JPL}^{Time}, ΔB_{UCAR}^{Time}, and ΔB_{WEGC}^{Time} in the 8-30 km layer are -0.01%, -0.02%, 0.12%, 0.02%, -0.02%, and -0.08%, respectively.

- The mean standard deviations in the same layer for all centers are within 0.02%. For temperature anomalies, the global mean temperature time series anomalies in the 8-30 km layer for DMI, GFZ, JPL, UCAR, and WEGC are 0.15 K, 0.0 K, -0.27 K, 0.04 K, and 0.09 K, respectively. The variation (standard deviation) of time series anomalies for each individual center are as small as 0.04 K (DMI), 0.06K (GFZ), 0.05K (JPL), 0.04K (UCAR) and 0.04K (WEGC), respectively.

3. Presentations and Publications

Related presentations and publications from January to December 2011 are listed:

1) Ho, S.-P., G. Kirchengast, S. Leroy, J. Wickert, A. J. Mannucci, A. K. Steiner, D. Hunt, W. Schreiner, S. Sokolovskiy, C. O. Ao, M. Borsche, A. von Engeln, U. Foelsche, S. Heise, B. Iijima, Y.-H. Kuo, R. Kursinski, B. Pirscher, M. Ringer, C. Rocken, and T. Schmidt 2010: Estimates of the Uncertainty for using Global Positioning System Radio Occultation Data for Climate Monitoring: Inter-comparisons of matched profiles (to be submitted)

2) Biondi, R., S.-P. Ho, W. Randel, T. Neubert, and S. Syndergaard, Tropical cyclone cloud top detection using the GPS bending angle, Atmospheric Chemistry and Physics (under review).

3) Biondi, R., W. Randel, S.-P. Ho, T. Neubert, and S. Syndergaard, 2011: Thermal structure of convective clouds using the GPS radio occultations (to be submitted).

4) Zeng, Zhen, S.-P. Ho, S. Sokolovskiy, The Structure and Evolution of Madden-Julian Oscillation from FORMOSAT-3/COSMIC Radio Occultation Data, *J. Geophy. Research (*to be submitted).

5) A. K. Steiner, D. Hunt, S.-P. Ho, G. Kirchengast, A. J. Mannucci, B. Scherllin-Pirscher, H. Gleisner, A. von Engeln, T. Schmidt, C. Ao, S. S. Leroy, E. R. Kursinski, U. Foelsche, M. Gorbunov, Y.-H. Kuo, K. B. Lauritsen, C. Marquardt, C. Rocken, W. Schreiner, S. Sokolovskiy, S. Syndergaard, and J. Wickert,Quantification of Structural Uncertainty in Climate Data Records from GPS Radio Occultation, GRL (to be submitted).

6) R. Biondi, S.-P. Ho, S. Syndergaard, T. Neubert, Tropical Cyclone Detection using GPS Radio Occultation Data, IUGG XXV General Assembly Earth on the Edge: Science for a Sustainable Planet, Melbourne, Australia 27 June - 8 July 2011.

7) Ricardo Biondi, S.-P. Ho, Convective Systems Analysis using GPS Radio Occultation, 3rd International Colloquium - Scientific and Fundamental Aspects of the Galileo Programme 31 August - 2 September 2011, Copenhagen, Denmark.

8) Ho, S.-P., Assessment of Systematic Biases of Radiosonde Moisture Measurements using Global Positioning System Radio Occultation from COSMIC, GEWEX/ESA DUE GlobVapour workshop on long term water vapour data sets and their quality assessment, 8 – 10 March 2011, ESA/ESRIN, Frascati, Italy (invited).

9) Ho, S.-P., Xinjia Zhou, Ying-Hwa Kuo, Assessment of Systematic Biases of Radiosonde Moisture Measurements using Global Positioning System Radio Occultation from COSMIC, 91st American Meteorological Society Annual Meeting, Seattle, WA, USA.

10) Callaghan, P. F., S.-P. Ho, T. Yunck, B. D. Wilson, and G. Manipon, 2011: Evaluation of AIRS V5 Temperature Profiles Using Matched Retrievals From COSMIC and ECMWF Analyses. Presentation, 91st American Meteorological Society Annual Meeting, Seattle, WA, USA.

11) Ho, S.-P., Xinjia Zhou, Ying-Hwa Kuo, Climate Calibration Observatory in Orbit: Using COSMIC RO Data to Calibrate and Validate the AIRS and AMSU Troposphere and Stratosphere Temperature Climate Data Records, 91st American Meteorological Society Annual Meeting, Seattle, WA, USA.

12) Steiner, A. K., S.-P. Ho, D. Hunt, G. Kirchengast, A. J. Mannucci, B. Scherllin-Pirscher, H. Gleisner, A. von Engeln , T. Schmidt C. Ao , S. S. Leroy , U. Foelsche , Y-H. Kuo , E. R. Kursinski, K. B. Lauritsen , S.

Syndergaard , C. Marquardt, C. Rocken, W. Schreiner, S. Sokolovskiy, J. Wickert W.and Coauthors, 2011: Uncertainty of the CHAMP Climate Record from Different Data Centers. The 5th FORMOSAT-3/COSMIC Data Users Workshop & ICGPSRO, April 12-14, 2011, Taipei, Taiwan.

13) Ho, S.-P., Y.-H. Kuo, X.-J. Zhou, and P. Callaghan, 2011: Long Term Assessment of Radiosonde Temperature Systematic Biases using COSMIC, CHAMP, and GRACE from 2001 to 2010. The 5th FORMOSAT-3/COSMIC Data Users Workshop & ICGPSRO, April 12-14, 2011, Taipei, Taiwan.

14) Zeng, Zhen, S.-P. Ho, S. Sokolovskiy, The Structure and Evolution of Madden-Julian Oscillation from FORMOSAT-3/COSMIC Radio Occultation Data. The 5th FORMOSAT-3/COSMIC Data Users Workshop & ICGPSRO, April 12-14, 2011, Taipei, Taiwan.

15) Barbara Scherllin-Pirscher, S.-P. Ho, Chia Chou, Ying-Hwa Kuo, Reconstruction of the 3-dimensional structure of ENSO using radio occultation data, The 5th FORMOSAT-3/COSMIC Data Users Workshop & ICGPSRO, April 12-14, 2011, Taipei, Taiwan.

16) Wen-Xin Deng, S.-P. Ho, Ching-Yuang Huang, Global and Regional Distribution of Water Vapor from COSMIC, , the 5th FORMOSAT-3/COSMIC Data Users Workshop & ICGPSRO, April 12-14, 2011, Taipei, Taiwan.

17) Raj, Jerry, Ching-Yuang Huang, S.-P. Ho, Jens Wickert, and Torsten Schmidt, Characteristics of Tropopause Height in Indian Monsoon Region Revealed by COSMIC GPS RO Data, the 5th FORMOSAT-3/COSMIC Data Users Workshop & ICGPSRO, April 12-14, 2011, Taipei, Taiwan.

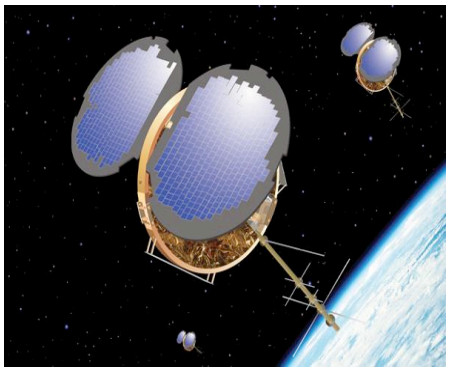

COSMIC

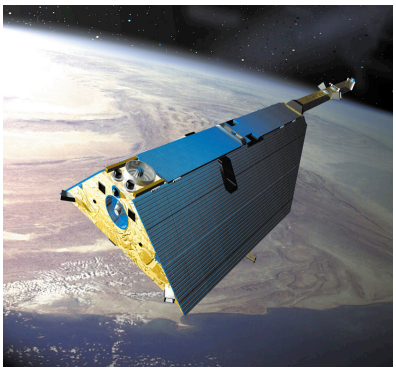

CHAMP

YEAR 2 BI-ANNUAL PROJECT REPORT (from 12/01/2011 to 05/31/2012)
NOAA Award number: NA10NES4400002

Construction of Consistent Microwave Sensor Temperature Records and Tropopause Height Climatology using MSU/AMSU Measurements, GPS RO Data, and Radiosonde Observations

Principal Investigator:
Shu-Peng (Ben) Ho (303-497-2922, spho@ucar.edu)

Co-Investigators:
Cheng-Zhi Zou ((301) 763-8042 x156, cheng-zhi.zou@noaa.gov)
Ying-Hwa Kuo **(**(303) 497-8910, kuo@ucar.edu)

National Center for Atmospheric Research
P.O. Box 3000, Boulder, CO 80307 USA

1. Introduction

In this study, we propose to carry out three tasks:

(i) To use GPS RO data from 2001 to 2012 as climate benchmark datasets to quantify the Microwave Sounding Unit (MSU)/Advanced Microwave Sounding Unit (AMSU) temporal and spatial temperature anomalies and to construct MSU/AMSU temperature records from 1979 to 2012;

(ii) To generate a long-term climate quality temperature dataset by reprocessing thirty-three years (1979-2012) of MSU/AMSU data. The 'adjusted' MSU/AMSU data and identified RO-consistent radiosonde data in the period of 2001 to 2009 (from the previous study) and from 2009 to 2012 will serve as reference data to calibrate other overlapped MSU/AMSU data from 1979 to 2001;

(iii) To use GPS RO soundings collected from multi-RO missions but processed using a consistent processing package to construct tropopause height climatology from 2001 to 2012 that is consistent with changes in temperature and tropopause structure estimated by radiosondes.

In this report, we summarize the continuous efforts since the last report (submitted in December 2011) for this project. The work undertaken to date is detailed in Section 2. We list presentations and publications since December 2011 in section 3.

2. Progress on Proposed Studies

Continued efforts since the last report have focused on: 1) Quantifying the reproducibility of RO data for climate monitoring –the profile-to-profile (PPC) results, 2) Quantifying the structural uncertainty in climate data records from GPS RO – inter-center monthly mean climatology comparison, 3) Construction of global tropopause height climatology using GPS radio occultation data, 4) Refining AMSU Ch9 processing method, and 5) Refining AMSU Ch7 processing method.

2.1 Quantifying the Reproducibility of RO Data for Climate Monitoring –the profile-to-profile (PPC) results

To examine the claim that Global Positioning System (GPS) radio occultation (RO) data are useful as a benchmark dataset for climate monitoring, here we continue quantifying the structural uncertainties of retrieved profiles that result from different processing methods.

Possible error sources of RO-derived products include i) observation errors and ii) inversion errors. Observation errors in RO phase measurements are related to GPS RO signal strength combined with receiver noise for a particular RO mission and local multipath effect [Kursinski1997]. The observation errors consist of random and systematic errors that may be mission-dependent. Structural uncertainties of RO-retrieved variables for a particular RO mission are mainly due to the inversion errors, which include errors in precise orbit determination (POD), removal of clock fluctuations, and other inversion procedures. While the fundamental phase measurement is synchronized to the ultra-stable atomic clocks on the ground, the RO-derived variables (e.g., refractivity, pressure, temperature) are not. The retrieval results may differ for different processing algorithms and implementations as used in the excess phase processing and inversion procedures, such as noise filtering and profile initializations (Ho et al., 2009).

Currently, multi-year GPS RO data can be obtained from the following centers: the Radio Occultation Meteorology (ROM) Satellite Application Facility (SAF) (formerly GRAS (Global Navigation Satellite System Receiver for Atmospheric Sounding) SAF) at the Danish Meteorological Institute (DMI) in Copenhagen, Denmark; the European Organisation for the Exploitation of Meteorological Satellites (EUMETSAT, hereafter EUM), in Darmstadt, Germany; the German Research Centre for Geosciences (GFZ) in Potsdam, Germany; the Jet Propulsion Laboratory (JPL) in Pasadena, CA, USA; the University Corporation for Atmospheric Research (UCAR) in Boulder, CO, USA; and the Wegener Center/University of Graz (WEGC) in Graz, Austria. These centers use different assumptions, initializations, and implementations in the excess phase processing and inversion procedures. These processing steps include: i) POD and atmospheric excess phase processing, ii) bending angle calculation, iii) ionospheric correction, iv) optimal estimation of the bending angles in the stratosphere, v) calculation of refractivity by Abel inversion, vi) calculation of pressure, temperature, and geopotential height, and vii) quality control (QC). Table 1 summarizes the retrieval methods used in this study for each processing step for the individual centers.

Table 1. Overview on implementations of processing chains at DMI, EUM, GFZ, JPL, UCAR, and WEGC.

URL/ Processing step	**Implementations for each center**
URL	**DMI :** *http://www.romsaf.org* **EUM** : *http://www.eumetsat.int* **GFZ** : *http://isdc.gfz-potsdam.de* **JPL** : *http://genesis.jpl.nasa.gov* **UCAR**: *http://www.cosmic.ucar.edu* **WEGC**: *http://www.wegcenter.at/globclim*
POD phase and orbit data	**DMI :** UCAR CDAAC orbit and phase data used (version 2009.2650). **EUM :** UCAR CDAAC orbit and phase data used (version 2009.2650). **GFZ** : POD: EPOS-OC for Rapid Science Orbit provision [*König et al.,* 2006]; Excess Phase: Single differencing, reference link smoothing. **JPL** : POD: reduced-dynamic strategy using GIPSY software [*Bertiger et al.,*1994]; Excess Phase: Double differencing.

	UCAR: POD computed with Bernese 5.0 software [*Dach et al.,* 2007]; Excess Phase: Single differencing, reference link smoothing. **WEGC**: UCAR CDAAC orbit and phase data used (version 2009.2650).
Bending angle calculation	**DMI:** Canonical Transform of Type 2 (CT2) inversion [*Gorbunov and Lauritsen*, 2004] below 25 km, combined with GO used above 25 km. **EUM:** Geometric optics used for BAs at all heights **GFZ** : Full Spectrum Inversion (FSI) below 15 km [*Jensen et al.,* 2003]; Geometric optics used above 15 km. **JPL** : Canonical transform (CT) after *Gorbunov* (2002) applied to L1. **UCAR**: FSI (Jensen et al., 2003) applied to L1 in troposphere < dynamic L2 QC height; Geometric optics used > dynamic L2 QC height. **WEGC**: Geometric optics used for L1 and L2 BAs at all heights.
Ionospheric correction	**DMI:** Optimal linear combination of L1 and L2 BAs [*Vorob'ev and Krasil'nikova*, 1994; *Gorbunov,* 2002]; Iono. correction term extrapolation < dynamic L2 QC height. Linear combination of L1 and L2 BAs [*Vorob'ev and Krasil'nikova*, 1994]. **EUM:** Linear combination of L1 and L2 BAs [*Vorob'ev and Krasil'nikova,* 1994]. **GFZ** : Linear combination of L1 and L2 BAs [*Vorob'ev and Krasil'nikova,* 1994], **JPL** : Linear comb. of L1 and L2 BAs [*Vorob'ev and Krasil'nikova,* 1994]; Iono. correction term extrapolation below 10 km. **UCAR**: Linear comb. of L1 and L2 BAs [*Vorob'ev and Krasil'nikova,* 1994]; Iono. correction term extrapolation < dynamic L2 QC height. **WEGC**: Linear comb. of L1 and L2 BAs [*Vorob'ev and Krasil'nikova,* 1994]; Iono. correction term extrapolation < 15 km.
Initialization of bending angles	**DMI:** Optimization after *Gorbunov* (2002), but using a two-parameter fit of background (MSISE-90) to data above 40 km in combination with a global background search [*Lauritsen et al.,* 2011]. Dynamic estimation of obs. errors [*Gorbunov,* 2002]; background error fixed at 50%. **GFZ** : Optimization after *Sokolovskiy and Hunt* [1996] with MSISE-90 (> 40 km). **JPL** : Exponential function fit at 40–50 km and extrapolation above. **UCAR**: Optimization after *Sokolovskiy and Hunt* [1996] with fitting backgr. prof. (NCAR clim. extrap. to 150 km), dynamic estimation of the top fit height, background and obs. errors [*Lohmann* 2005]. **WEGC:** Statistical optimization > 30 km with ECMWF analyses and MSISE-90 to 120 km [*Healy*, 2001], dynamic estimation of obs. errors and inverse covariance weighting [*Gobiet and Kirchengast,* 2004; *Gobiet et al.,* 2007].
Derivation of refractivity	**DMI:** Numerical calculation of the Abel integral [*Fjeldbo et al*., 1971] from each height to 150 km. **GFZ** : Abel inversion of the optimized bending angle profiles starts at 150 km.. **JPL** : Able inversion of the ionosphere-corrected bending angle from each height up to 120 km. **UCAR**: The optimized bending angle is subjected to Abel inversion below 150 km by applying the finite-difference representation [*Sokolovskiy et al*., 2005]. **WEGC**: Numerical integration over bending angle (Simpson's trapezoidal rule) from each height (impact par.) to 120 km. Impact par. to height conversion with radius of curvature at mean TP location [*Syndergaard*, 1999]; Sinc-windowed Blackman filter on refractivity (< 1 km moving average, for resolution-conserving filtering of residual numerical processing noise).
Dry air retrieval	**DMI:** Refractivity is directly proportional to air density (applying ideal gas equation). Pressure downward integration of the hydrostatic equation from 150 km (boundary conditions determined from the refractivity and its gradient at the top); Dry geopotential height relative to EGM-96; Temperature: Smith-Weintraub formula for dry air [*Smith and Weintraub*, 1953]. **GFZ** : Pressure retrieval is initialized at 100 km with MSISE-90. Pressure downward integration using hydrostatic equation. ; Dry geopotential height relative to EGM-96; Dry temperature after Smith-Weintraub eq. and eq. of state. **JPL** : Pressure integration using hydrostatic equation starting at 40 km. Dry geopotential height relative to JGM-3. Dry temperature after Smith-Weintraub eq. and eq. of state, temperature initialization using ECMWF temperature at 40 km. **UCAR**: Pressure integration using hydrostatic equation, initialized at 150 km by setting pressure and temperature to zero. Dry temperature after Smith-Weintraub eq. and eq. of state. **WEGC**: Hydrostatic integral initialization at 120 km, pressure = pressure(MSISE-90); no initialization below 120 km (downward integration); Dry geopotential height relative to EGM-96; Smith-Weintraub eq. and eq. of state (ideal gas) to obtain dry temperature; Same filtering on dry temperature as for refractivity filtering.
Quality control	**DMI:** QC of L2 quality from impact parameters (noise); QC of BA using model from iono. corr.; QC of N using ECMWF analyses: reject if $\Delta N > 10$ % in 10–45 km. **GFZ** : QC of forward differences of excess phases and QC of bending angles; QC of N using MSISE-90: reject if $\Delta N > 22.5$ %. **JPL** : QC of Doppler shift < 6km; QC of N, T <30 km: ECMWF analyses, >10% ΔN and >10 K ΔT rejected. **UCAR**: QC of raw L1 Doppler (truncation); QC of L2 Doppler (reject if dynamic QC height > 20 km); QC of bending angle (reject if top fit height < 40 km); QC of N using climatology (reject if difference > 50%).

	WEGC: QC of excess phases and bending angles; QC of N, T using ECMWF analyses: reject if ΔN > 10 % in 5–35 km and/or ΔT > 20 K in 8–25 km.

In this study, we conduct profile-to-profile comparisons of CHAMP (CHAllenging Minisatellite Payload) data from January 2002 to August 2008 retrieved by six RO processing centers. Differences and standard deviations of the individual centers relative to the inter-center mean are used to quantify the structural uncertainty. Uncertainties accumulate in derived variables due to propagation through the RO retrieval chain. This is reflected in the inter-center differences, which are small for bending angle and refractivity increasing to dry temperature, dry pressure, and dry geopotential height.

To estimate the reproducibility of RO data, in this study we quantify i) the structural uncertainties, and ii) long-term consistency of retrieved profiles that result from different processing methods. Here we conduct profile-to-profile comparisons (PPCs) (i.e., contain no sampling differences) to quantify the structural uncertainties of RO-retrieved variables and to understand how those uncertainties propagate from bending angle profiles to pressure and temperature profiles. This should help identify the causes of process-dependent errors from each center.

Results show that the mean differences of the time series in the 8 km to 30 km layer range from –0.08% to 0.12% for bending angle, –0.03% to 0.02% for refractivity, –0.27 K to 0.15 K for dry temperature, –0.04% to 0.04% for dry pressure, and –7.6 m to 6.8 m for dry geopotential height. The corresponding standard deviations are within 0.02%, 0.01%, 0.06 K, 0.02%, and 2.0 m, respectively. The mean trend differences from 8 km to 30 km for bending angle, refractivity, dry temperature, dry pressure, and dry geopotential height are within ±0.02%/5yrs, ±0.02%/5yrs, ±0.06 K/5yrs, ±0.02%/5yrs, and ±2.3 m/5yrs, respectively. Although the RO-derived variables are not readily traceable to the international system of units, the high precision nature of the raw RO observables is preserved in the inversion chain.

Figure 1 depicts the de-seasonalized temperature anomalies for DMI, GFZ, JPL, UCAR, and WEGC ($\Delta T_{\mathrm{DMI}}^{\mathrm{Deseason}}$, $\Delta T_{\mathrm{GFZ}}^{\mathrm{Deseason}}$, $\Delta T_{\mathrm{JPL}}^{\mathrm{Deseason}}$, $\Delta T_{\mathrm{UCAR}}^{\mathrm{Deseason}}$, and $\Delta T_{\mathrm{WEGC}}^{\mathrm{Deseason}}$) for the northern mid-latitudes, the Tropics, and the southern high-latitudes. Left panels are for the 12 km to 20 km layer, and the right panels are for the 20 km to 30 km layer. The temperature anomalies for other latitudinal zones are similar to those in Fig. 14 and are not shown here. The trends for $\Delta T_{\mathrm{DMI}}^{\mathrm{Deseason}}$, $\Delta T_{\mathrm{GFZ}}^{\mathrm{Deseason}}$, $\Delta T_{\mathrm{JPL}}^{\mathrm{Deseason}}$, $\Delta T_{\mathrm{UCAR}}^{\mathrm{Deseason}}$, and $\Delta T_{\mathrm{WEGC}}^{\mathrm{Deseason}}$ in the 12 km to 20 km layer agree within ±0.03 K/5yrs, because their differences are constant over time with a standard deviation of 0.03 K. The global trend differences for each center in the 8 km to 12 km layer are within ±0.02 K/5yrs and within ±0.06 K/5yrs in the 8 km to 30 km layer.

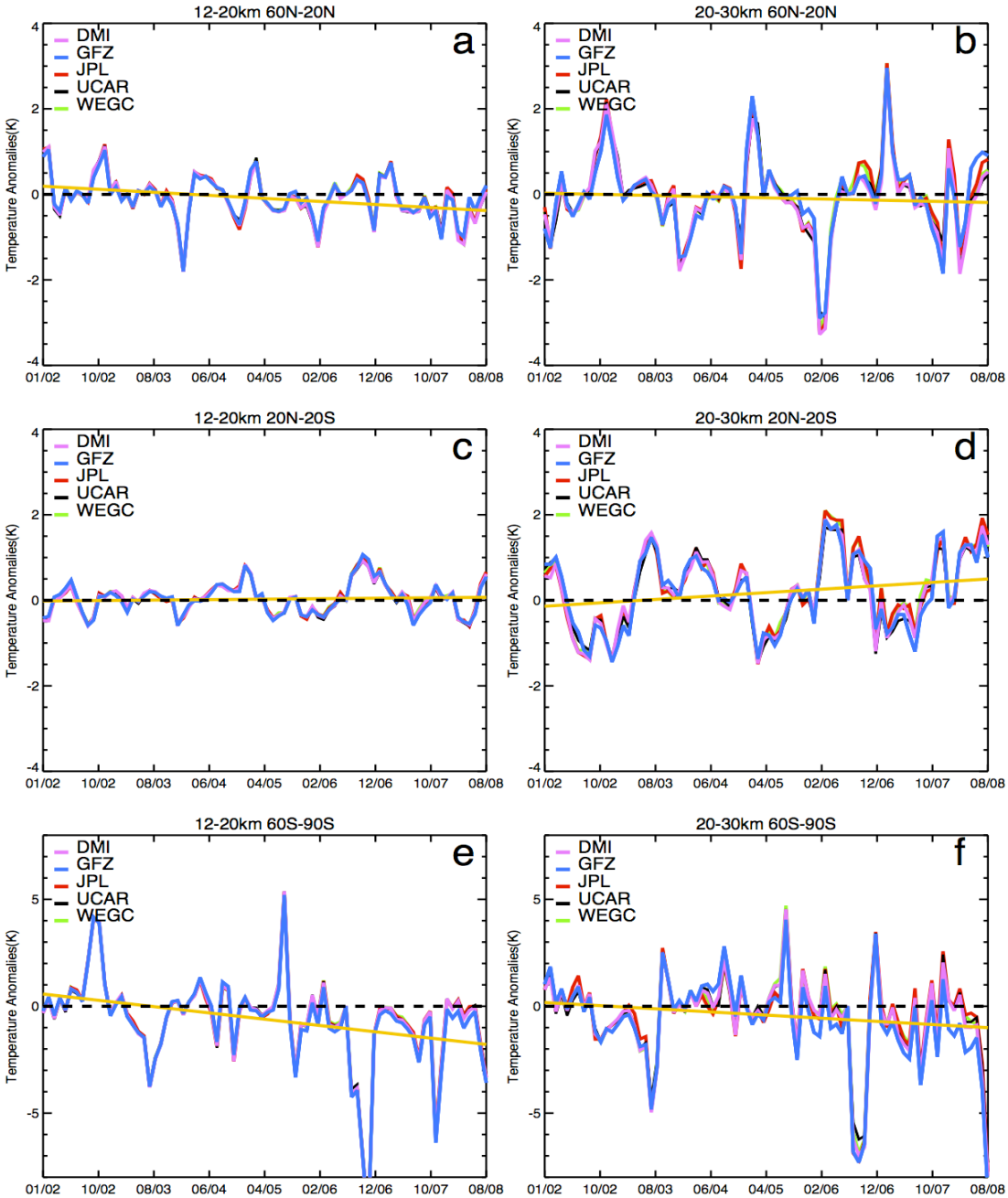

Fig. 1. The de-seasonalized temperature anomalies for each center in the 12 km to 20 km layer for (a) the 60ºN to 20ºN zone, (c) the 20ºN to 20ºS zone, and (e) the 60ºS to 90ºS zone, and in the 20 km to 30 km layer for (b) the 60ºN to 20ºN zone, (d) the 20ºN to 20ºS zone, and (f) the 60ºS to 90ºS zone. The 5-yr trend of the inter-center mean is shown as well. Note that the ordinate range of panels e and f is enlarged to ±8 K (relative to ±4 K of panels a-d).

2.2 Quantifying the Structural Uncertainty in Climate Data Records from GPS RO – Inter-center Monthly Mean Climatology Comparison

To use RO data as a benchmark dataset for climate monitoring, it is critically necessary to quantify the reproducibility of RO retrieved profiles as well as the structural uncertainty in the climate data records (i.e., monthly mean climatologies). The reproducibility of RO data is defined by the consistency (small structural uncertainty) of i) global averages, ii) monthly zonal averages, and iii) anomaly time series of the RO retrieval profiles among centers due to different assumptions and inversion methods. A first study to this end was performed by Ho et al., (2009) who used five years (2002 to 2006) of refractivity climatologies from CHAMP generated by GFZ, JPL, UCAR, and WEGC. Each center used the profiles that passed their own quality control criteria to generate monthly mean climatologies. Results showed that the uncertainty of the trend for the fractional refractivity anomalies among the centers is between (–0.03 to 0.01)%/5yrs.

To further quantify the structure uncertainty in climatology data records from GPS RO data, we further examine the monthly mean climatology (MMC) differences generated by DMI, EUM, GFZ, JPL, UCAR, and WEGC. Results show that the mean standard deviation of trends is 0.02% for bending angle, 0.02% for refractivity, 0.03% for pressure, <3 m for geopotential height, and 0.05 K for temperature. Structural uncertainty increases above 25 km and at high latitudes, mainly due to different bending angle initialization approaches in the centers' processing schemes including different background information. At high-latitudes larger residual sampling error due to higher atmospheric variability is also an influence factor. The uncertainties found are consistent with those of a former refractivity-only study over five years (Ho2009), and with those of a parallel individual-profile-based RO inter-comparison study (Ho et al., 2012), confirming the suitability of RO climatologies by accounting for the sampling error.

2.3 Construction of Global Tropopause Height Climatology using GPS Radio Occultation Data

The tropopause represents the boundary between the tropopause and stratosphere. It is an important region of the atmosphere often been examined to understand the stratosphere-troposphere exchange and coupling. Continued efforts are made to use GPS RO soundings collected from multi-RO missions but processed using a consistent processing package to construct tropopause height climatology from 2001 to 2012. Results for a) inter-comparing the tropopasue height climatology derived from different RO missions, and b) quantifying the structural uncertainty of tropopause height derived from GPS radio occultation data are summarized in this section.

a. Inter-comparison of the Tropopause Height Climatology derived from different RO Missions

Here we continue deriving tropopause height (lapse rate tropopasue (LPT) and cold point tropopause (CPT)) cliamtolgies from individual RO missions. These include CHAMP (2001 to 2008), GPS/Meteorology (GPS/MET, from 1995 to 1997), COSMIC (launched in April 2006), Gravity Recovery And Climate Experiment (GRACE, launched in 2004), Satélite de Aplicaciones Científicas-C (SAC-C, launched in 2000), MetOp/GRAS (launched in 2006), Communication/Navigation Outage Forecast System (C/NOFS, launched in 2008), and Terra Synthetic Aperture Radar (SAR) operating in the X-band (TerraSAR-X, launched in 2007). Figure 2 show the monthly mean tropopasue height differences between COSMIC and CHAMP from June 2006 to the September 2008.

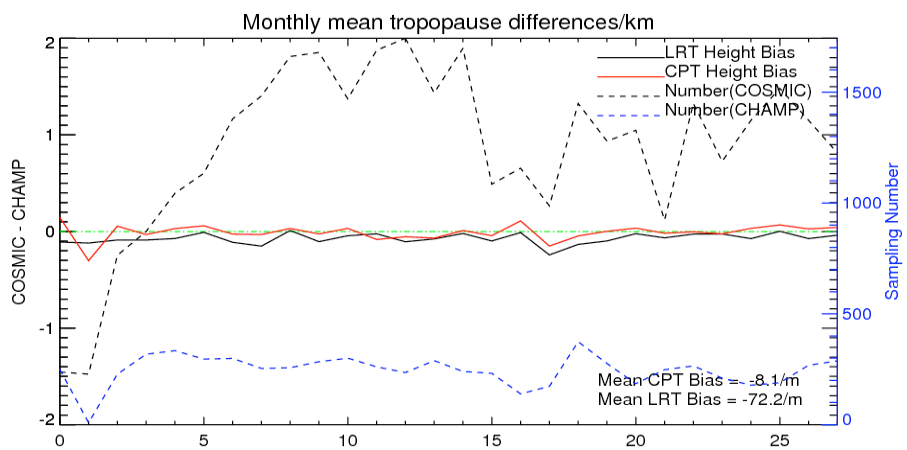

Figure 2. The monthly mean CPT and LRT differences between COSMIC and CHAMP during the period from June 2006 to September 2008.

b. Estimating the structural uncertainty of tropopause height derived from GPS radio occultation data

We continue quantifying the structural uncertainty of tropopause height derived from GPS radio occultation data. This is to inter-compare the of CHAMP tropopause height derived from DMI, EUM, GFZ, JPL, UCAR, and WEGC. Figure 3 illustrates the results for the LRT height trends for the different binning methods and RO data centers. Results show that at most latitudes the LRT height trend is more sensitive to the binning method than the data centers. Although independent inversion algorithms and different quality control methods are used among centers, the difference among centers either for 5° or 10° binning method agree to within ±10m/yr except in the polar region. Polar region show the largest difference between data centers for 5° binning methods (especially in the south polar region). This can be explained with the small sampling number and not apparent minimum values for temperature profiles in polar region.

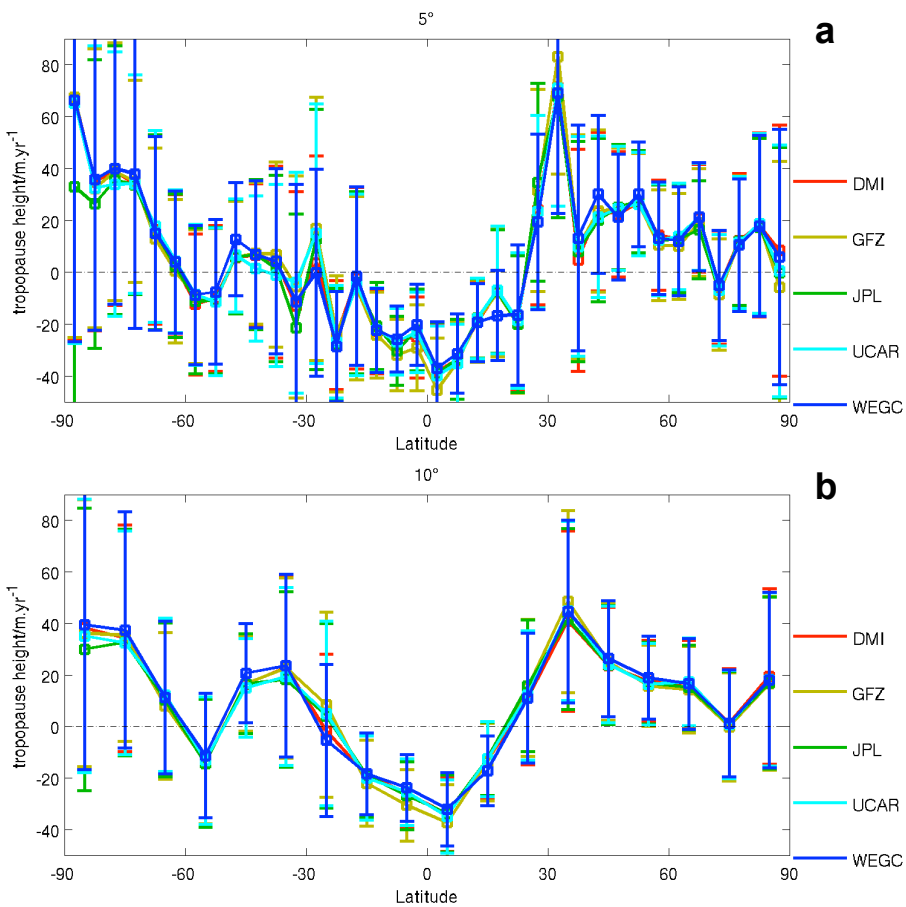

Figure 3. Annual LRT height trends deduced with different RO data centers and (a) 5° or (b) 10° binning method. Error bars denote the ±2-sigma confidence intervals.

2.4 Refining AMSU Ch9 processing method

During this performance period (from Dec. 2011 to May 31, 2012), we continue to refine the AMSU Ch9 brightness temperatures (temperature in the lower stratosphere, TLS) processing method. The refining procedures are mainly focusing on i) Identification and calibration of inter-satellite bias, ii) Identification and calibration of location and time dependent biases, and iii) Long term correction of the combined effect of the drift of the satellite orbit and the location and time dependent biases.

Approaches:

- Refining the method to use GPS RO simulated TLS to calibrate AMSU TLS from multiple NOAA missions (NOAA 15, 16, 18, 19), Metop-A AMSU, and Aqua AMSU
- Refining the method to applying RO calibrated AMSU TLS to calibrate MSU ch4 (from NOAA 14 etc.)

Results:

Figure 4 shows the monthly mean biases between NOAA 15 TLS and RO calculated TLS when they are collocated (black line). The blue line indicates the time series of monthly mean biases between NOAA 15 TLS and that from RO data after calibration.

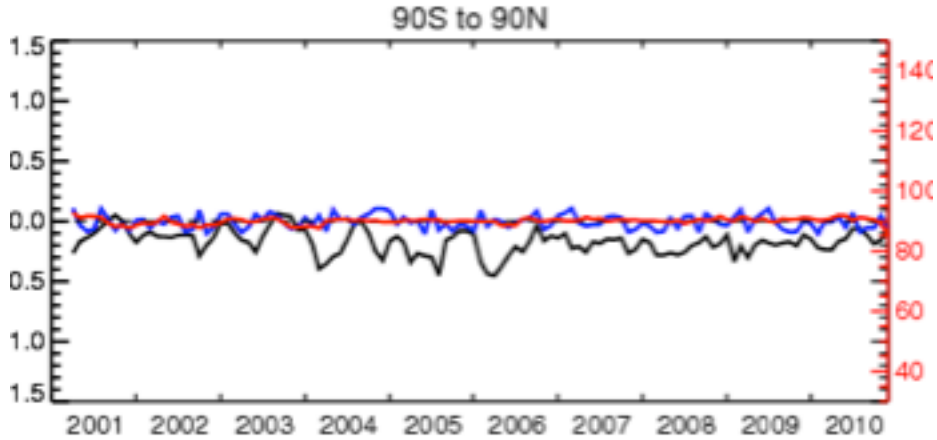

Figure 4. NOAA 15 TLS biases comparing to GPS RO calculated TLS before calibration (black line) and after calibration (blue line).

Figure 5 shows the time series of the inter-satellite TLS biases (raw data) relative to NOAA 15 from 2001 to 2010. Before calibration algorithms are applied, the inter-satellite biases among satellites (NOAA 15, 16, 18, 19, Metop-A, and Aqua) are obvious.

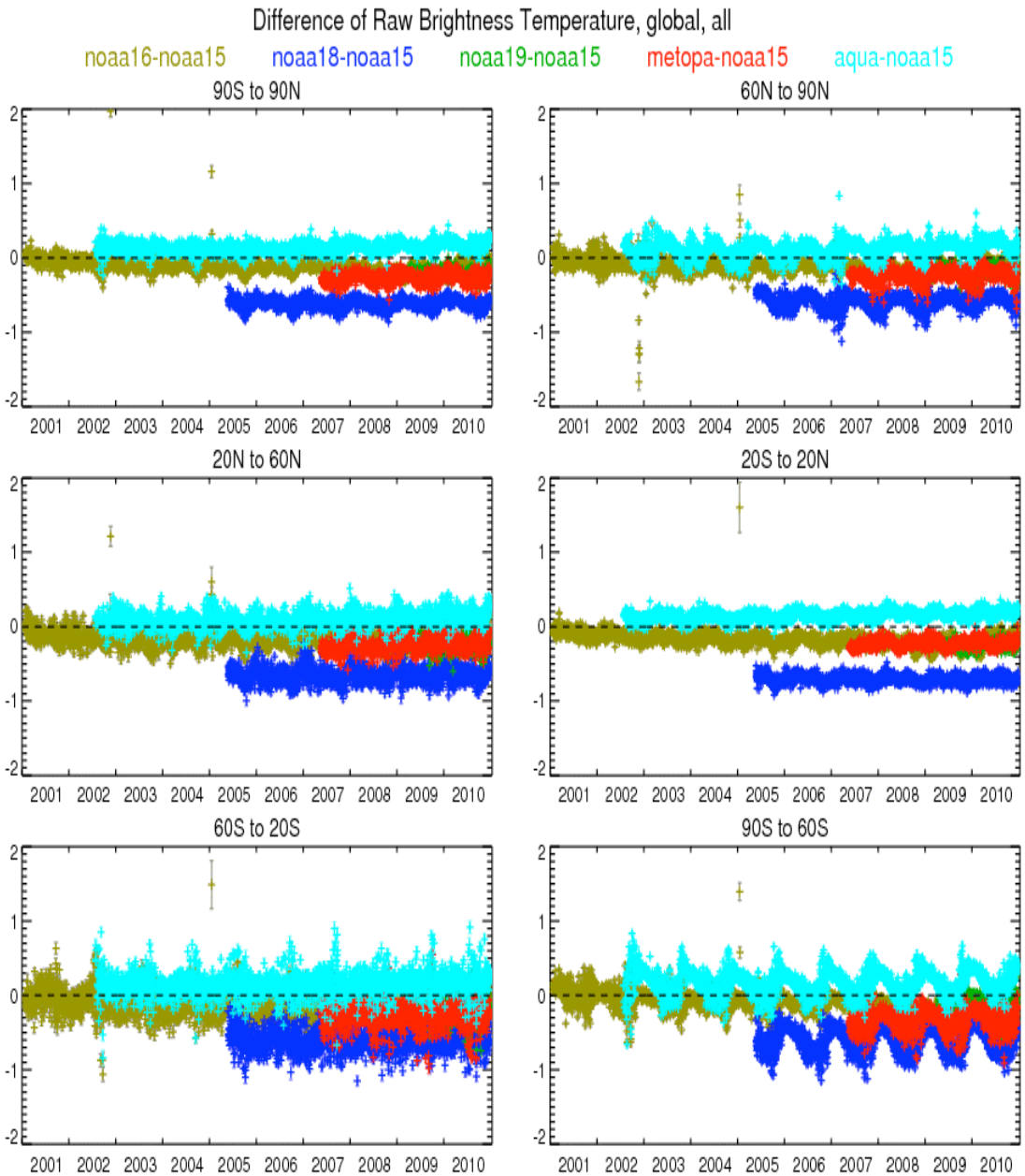

Figure 5. Time series of TLS differences of NOAA-NOAA15, NOAA18-NOAA15, NOAA19-NOAA15, Metop-A – NOAA15, and Aqua-NOAA15 for the global, 90°N-60°N, 60°N-20°N, 20°N-20°S, 20°S-60°S, and 60°S-90°S.

After using RO TLS to calibrate TLS for each satellite missions, the inter-satellite among missions are within ±0.3K globally (Figure 6).

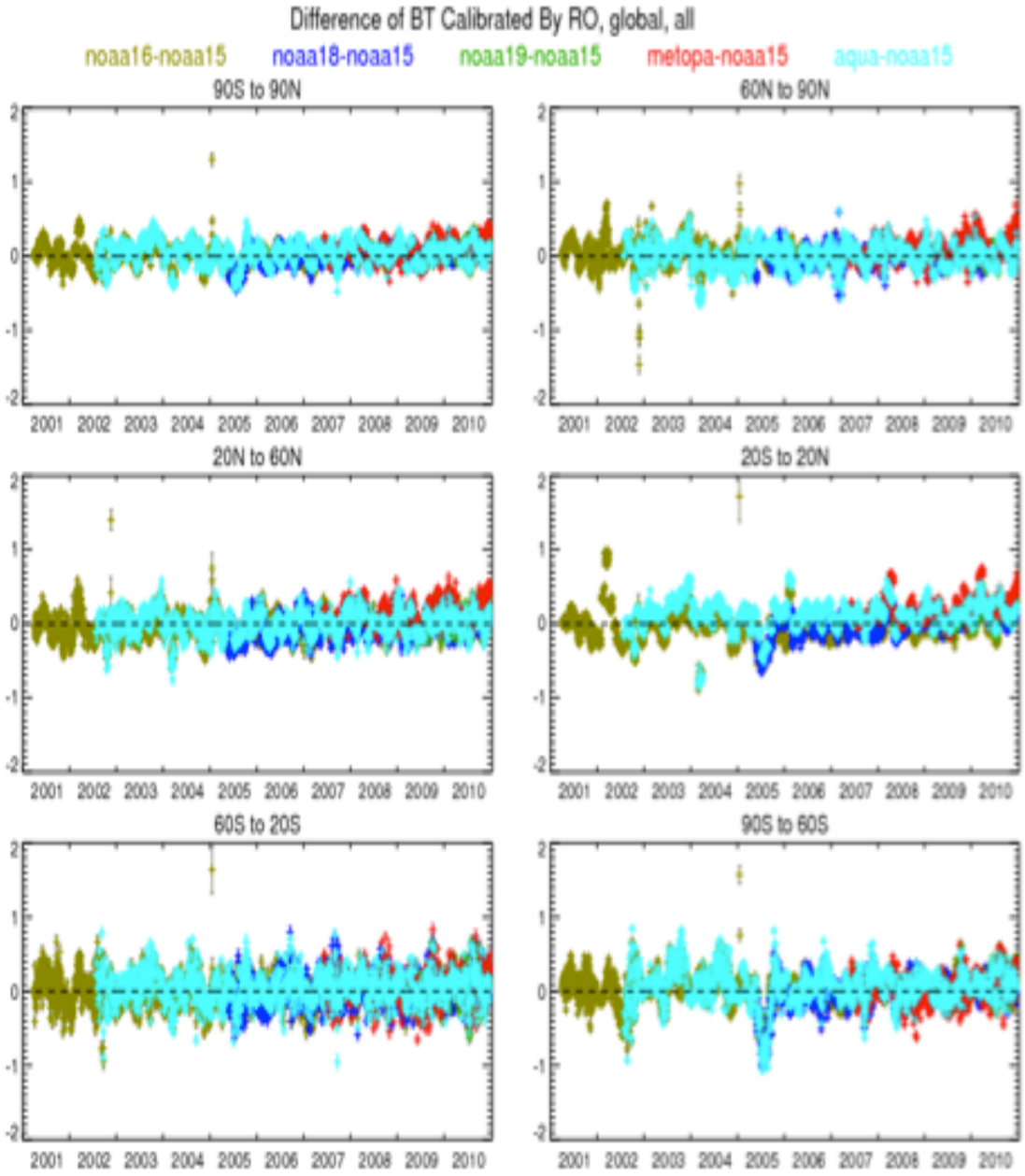

Figure 6. Time series of RO calibrated TLS differences of NOAA-NOAA15, NOAA18-NOAA15, NOAA19-NOAA15, Metop-A – NOAA15, and Aqua-NOAA15 for the global, 90°N-60°N, 60°N-20°N, 20°N-20°S, 20°S-60°S, and 60°S-90°S.

2.5 Refining AMSU ch7 calibration algorithm

In the performance period, we continue refining the AMSU ch7 calibration algorithm. Because RO temperature is less affected by moisture amount above 8 km, we first use RO temperature profiles to collocate with different radiosonde (RAOB) types and identify high quality of ROAB data and use those data to calibrate AMSU ch7 Tbs from different satellite missions. Figure 7 shows time series of monthly mean temperature bias between radiosonde of Vaisala RS92 and GPS RO data at 50 hPa. In general, temperature measurements from RS92 are in general very consistent with those of collocated RO temperature. Except in the Tropics, the mean biases between RS92 and RO temperatures are within ±0.25K.

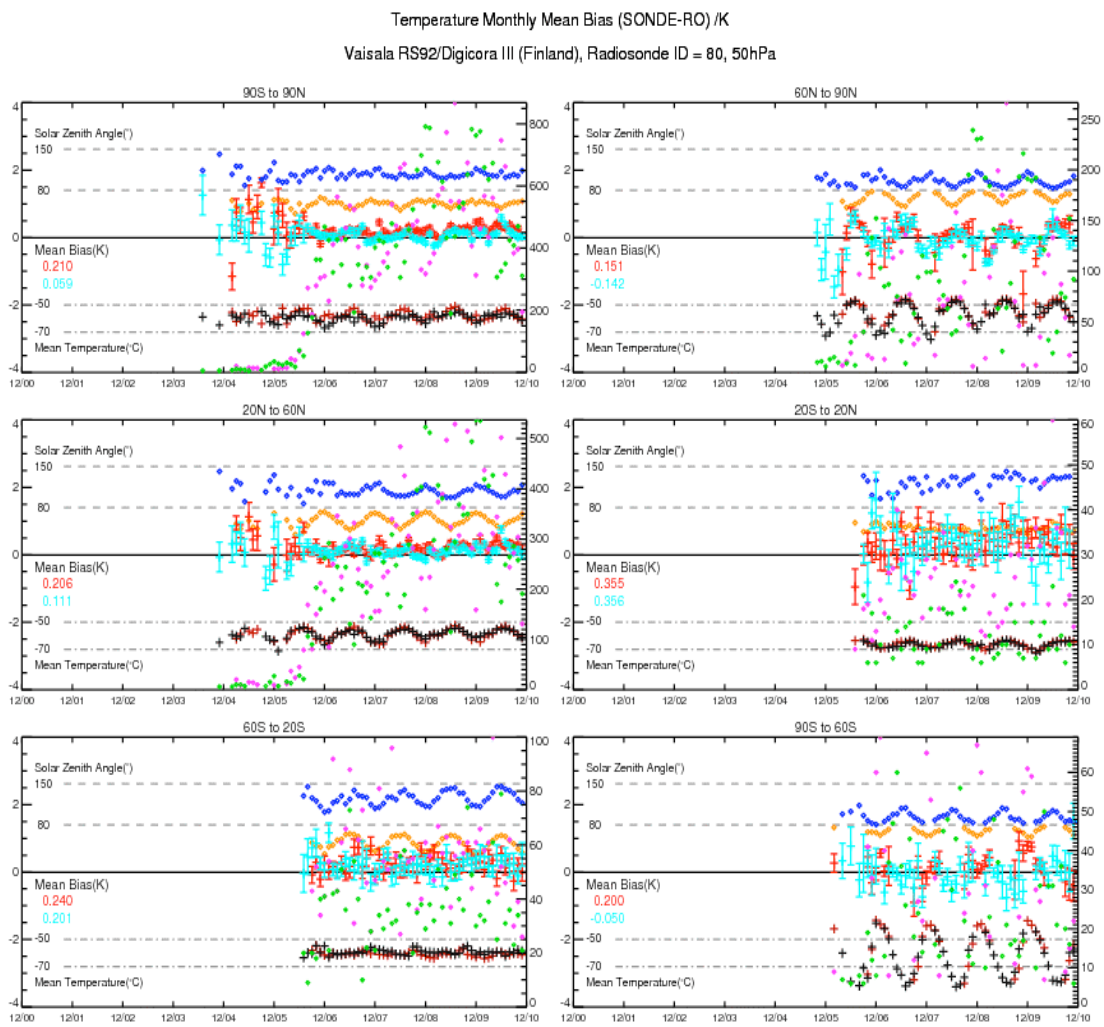

Figure 7. The differences of temperature between RS92 and collocated GPS RO at 50 hPa for the global (upper left panel), 90º N to 60º N zone (upper right panel), 20º N to 60º N zone (middle left panel), 20º N to 20º S zone (middle right panel), 60º S to 20º S zone (lower left panel), and 90º S to 60º S zone (lower right panel).

Using identified RAOB types from 2001 to 2010, we compute the forward calculated AMSU ch7 Tbs and use the RAOB calculated AMSU ch7 Tbs to calibrate AMSU ch7 Tbs from NOAA15, 16, 18, 19, Metop-A, and Aqua. After using RAOB calculated ch7 Tbs to calibrate those for AMSU ch7 Tbs for each satellite missions, the inter-satellite among missions are within ±0.5K globally (Figure 8).

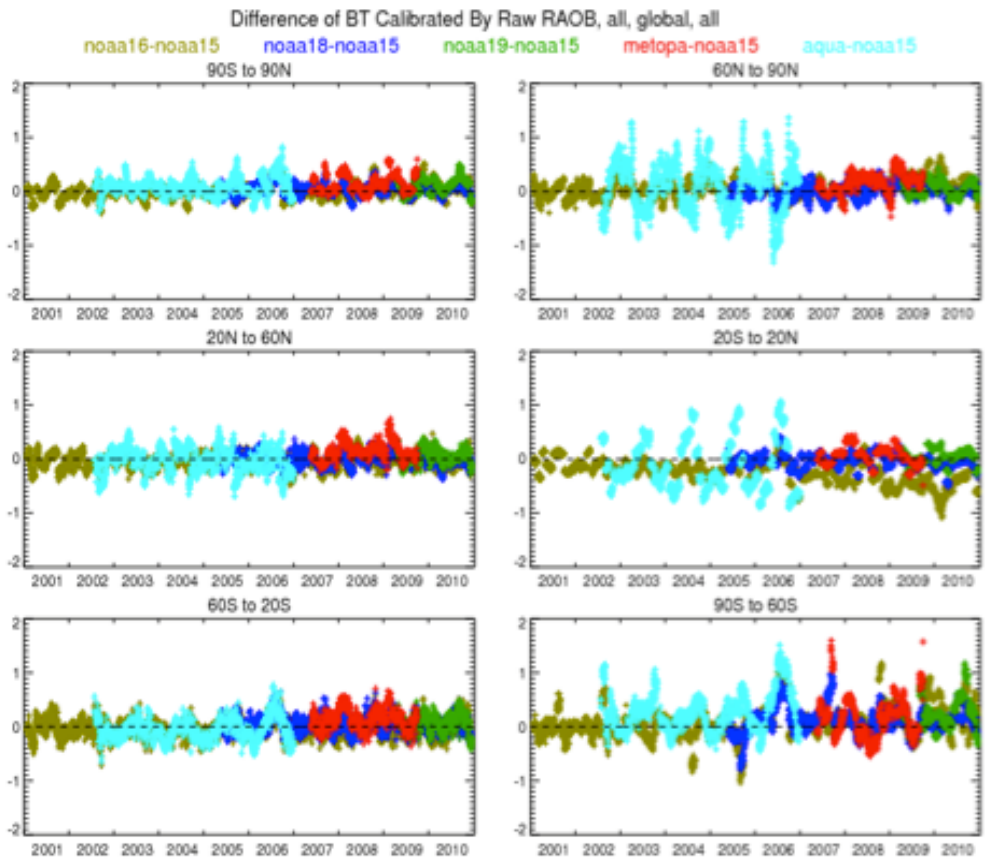

Figure 8. The time series of AMSU ch7 Tbs between NOAA-NOAA15, NOAA18-NOAA15, NOAA19-NOAA15, Metop-A – NOAA15 for the global (upper left panel), 90º N to 60º N zone (upper right panel), 20º N to 60º N zone (middle left panel), 20º N to 20º S zone (middle right panel), 60º S to 20º S zone (lower left panel), and 90º S to 60º S zone (lower right panel).

3. Presentations and Publications

Related presentations and publications from December 2011 to May 2012 are listed:

1) **Ho, S.-P.**, Doug Hunt, Andrea K. Steiner, Anthony J. Mannucci, Gottfried Kirchengast, Hans Gleisner, Stefan Heise, Axel von Engeln, Christian Marquardt, Sergey Sokolovskiy, William Schreiner, Barbara Scherllin-Pirscher, Chi Ao, Jens Wickert, Stig Syndergaard, Kent B. Lauritsen, Stephen Leroy, Emil R. Kursinski, Ying-Hwa Kuo, Ulrich Foelsche, Torsten Schmidt, and Michael Gorbunov (2012), Reproducibility of GPS Radio Occultation Data for Climate Monitoring: Profile-to-Profile Inter-comparison of CHAMP Climate Records 2002 to 2008 from Six Data Centers, *J. Geophys. Res*. 2012, (in press).

2) Mears C., J. Wang, **S.-P. Ho**, L. Zhang, and X. Zhou, Total Column Water Vapor, [In "States of the Climate in 2011]. *Bul. Amer. Meteor. Sci.,* 2012, in press (in press).

3) Steiner, A. K., D. Hunt, **S.-P. Ho**, G. Kirchengast, A. J. Mannucci, B. Scherllin-Pirscher, H. Gleisner, A. von Engeln, T. Schmidt, C. Ao, S. S. Leroy, E. R. Kursinski, U. Foelsche, M. Gorbunov, Y.-H. Kuo, K. B. Lauritsen, C. Marquardt, C. Rocken, W. Schreiner, S. Sokolovskiy, S. Syndergaard, and J. Wickert,Quantification of Structural Uncertainty in Climate Data Records from GPS Radio Occultation, *J. Geophys. Res.* 2012 (submitted).

4) Zeng, Zhen, **S.-P. Ho**, S. Sokolovskiy, The Structure and Evolution of Madden- Julian Oscillation from FORMOSAT-3/COSMIC Radio Occultation Data, *J. Geophy. Research,* (accepted).

5) Biondi, R., W. Randel, **S.-P. Ho**, T. Neubert, and S. Syndergaard, 2011: Thermal structure of intense convective clouds derived from GPS radio occultations, ACP, 2012 (accepted).

6) **Ho, S.-P.**, The Use of the COSMIC/FORMOSAT-3 Global Positioning System Radio Occultation Data as Global Reference Observations in Orbit and Their Applications in Meteorology, invited seminar given in National Central University, GPSARC, January 11, 2012, Taiwan (invited talk).

7) **Ho, S.-P.** and co-authors, Independent Assessment of Microwave Temperature in the Lower Stratosphere From 2001 to 2010 Using GPS RO Calibrated Microwave Temperature Climate Data Records: Using GPS RO Observations As a Climate Reference Dataset, 92nd American Meteorological Society Annual Meeting, January 23-26, New Orleans, LA, USA.

8) **Ho, S.-P.** and co-authors, The Reproducibility of GPS Radio Occultation for Climate Monitoring: Profile to Profile Inter-Comparison of CHAMP Climate Bending Angle, Refractivity, Temperature, and Geo-Potential Height Records 2002-2008 From Different Data Centers, 92nd American Meteorological Society Annual Meeting, January 23-26, New Orleans, LA, USA.

9) **Ho, S.-P.,** D. Hunt, A. K. Steiner, Anthony J. Mannucci, Gottfried Kirchengast, Hans Gleisner, Stefan Heise, Axel von Engeln, Christian Marquardt, Sergey Sokolovskiy, William Schreiner, Barbara Scherllin-Pirscher, Chi Ao, Jens Wickert, Stig Syndergaard, Kent B. Lauritsen, Stephen Leroy, Emil R. Kursinski, Ying-Hwa Kuo, Ulrich Foelsche, Torsten Schmidt, and Michael Gorbunov,, Summaries of GPS RO Inversion Procedures in the Upper Troposphere and Middle Stratosphere among Operational Centers and Structural Uncertainties in the Multiple Center Comparisons, 2nd IROWG Workshop 28 March 3, April 2012, Estes Park, CO, U.S.A.

10) Scherllin-Pirscher, B., C. Deser, **S.-P. Ho**, C. Chou, W. Randel, and Y.-W. Kuo Three dimensional reconstruction of the atmospheric El Niño-Southern Oscillation signal, 2nd IROWG Workshop 28 March 3, April 2012, Estes Park, CO, U.S.A.

11) Steiner, A. K., D. Hunt, **S.-P. Ho**, Anthony J. Mannucci, Gottfried Kirchengast, Hans Gleisner, Stefan Heise, Axel von Engeln, Christian Marquardt, Sergey Sokolovskiy, William Schreiner, Barbara Scherllin-Pirscher, Chi Ao, Jens Wickert, Stig Syndergaard, Kent B. Lauritsen, Stephen Leroy, Emil R. Kursinski, Ying-Hwa Kuo, Ulrich Foelsche, Torsten Schmidt, and Michael Gorbunov, Quantification of Structural Uncertainty in Climate Data Records from GPS Radio Occultation, 2nd IROWG Workshop 28 March 3, April 2012, Estes Park, CO, U.S.A.

12) Zhen, Zeng, **S.-P. Ho**, Sergey Sokolovskiy, Ying-Hwa Kuo, Intraseasonal variability of the tropical tropopause derived from COSMIC RO data, 2nd IROWG Workshop 28 March 3, April 2012, Estes Park, CO, U.S.A.